EarthArXiv Preprint Cover Sheet

This manuscript is a non-peer-reviewed preprint submitted to **EarthArXiv**. It has not been certified by peer review.

This manuscript has also been submitted for peer review to the **Planetary Science Journal (PSJ)**, published by the American Astronomical Society (AAS), under manuscript number **AAS77321** (submitted 23 May 2026). As of the date of this preprint, the manuscript is at the "*Seeking Scientific Editor*" stage and has not yet been assigned to peer reviewers.

Earlier and less developed versions of this work were previously deposited on Zenodo, OSF, and GitHub as preprint / open-science materials.

Subsequent revisions of this preprint may be posted to reflect the outcome of the peer-review process at PSJ.

Moon Formation by Triple Phase Transition in the Differentiating Proto-Earth

Michel Debailleul

Geophysicist

Université libre de Bruxelles (ULB)

ORCID: 0009-0003-1222-1433

michel.debailleul@yahoo.fr

2026

Abstract. The origin of the Moon remains one of the unresolved problems of planetary science. The canonical giant-impact model faces growing geochemical difficulties: it does not naturally predict the near-perfect Earth–Moon isotopic identity, the crustal dichotomy, or the ≈ 350 Myr delay of the terrestrial dynamo. This work proposes an alternative grounded in a necessary thermodynamic observation: any Earth-mass planet emerges from accretion in a state of near-total silicate mantle melting, with accretion energy exceeding total melting energy by a factor of ≈ 155 (Solomatov, 2000; Elkins-Tanton, 2012; Rubie et al., 2015). The proto-Earth is therefore a rapidly rotating ($T_{\rm rot} \approx 3.5$ h) magmatic body lacking a stabilizing satellite.

In the Hadean context — a T-Tauri Sun whose coronal mass ejections are 10 to 100 times more intense than today's (Feigelson & Montmerle, 1999; Airapetian et al., 2016), a dense silicate atmosphere at 2,000–4,000 K acting as a thermal blanket (Elkins-Tanton, 2008; Lebrun et al., 2013; Hamano et al., 2013), continuous planetesimal bombardment (Agnor et al., 1999; Kokubo & Genda, 2010), and active short-lived radioactivity (Urey, 1955; Huss et al., 2009) — the proto-Earth's axis undergoes large-amplitude free nutation within $[40°, 70°]$ in its own co-rotating frame (Laskar et al., 1993a; Laskar & Robutel, 1993b; Touma & Wisdom, 1993; Li & Batygin, 2014). This is *not* an astronomical obliquity relative to a non-existent Hadean ecliptic; it is a purely internal geometric oscillation of the fluid body.

In this context, a single engine — the progressive Fe-Ni segregation toward the forming core — governs three coupled transitions. The first is a rheological transition: the silicate magma acquires a Bingham-Herschel yield stress (Bingham, 1922; Herschel & Bulkley, 1926) and structures a Coherent Magmatic Torus (CMT) within the intertropical band $|\phi| < 30°$. The second is a mechanical transition: the CMT undergoes two to three episodes of hypersonic cohesive ejection beyond the Roche radius, governed by a double potential well and the stochastic Kramers crossing rate (Kramers, 1940). The third is a magnetic transition: the terrestrial dynamo switches on ≈ 350 Myr after the ejections cease, in agreement with the paleomagnetic data from Jack Hills zircons (Tarduno et al., 2025).

The central equation gives an ejected mass of 2.2–4.0×10^{22} kg per episode; with $N = 2$–3 episodes and a capture efficiency of 0.70, the lunar mass is reconstituted. The mechanism requires no external impactor and satisfies the isotopic identity, iron depletion, and angular momentum constraints as direct mechanical consequences.

The central prediction is one or more seismic interfaces between 200 and 530 km depth, with an impedance contrast $|R| \in [0.01, 0.04]$. This prediction is testable by **Chang'e 7** (South Pole, August 2026), **FSS** (Farside Seismic Suite), **LEMS** (Lunar Environment Monitoring Station), and **Artemis III** (2028–2029). Preliminary observational support is provided by Chang'e-6 samples (Yue et al., 2026; Xu et al., 2025): norites dated at 4247 ± 5 Ma (consistent with Episode 1) and anomalously high Fe/Mn ratios in deep olivines, both consistent with predictions P3 and P6 of this work. All hypotheses are explicit and hierarchized. Limitations are acknowledged. The validation program is defined and sequenced.

Interactive simulation: https://orion4622.github.io/moon-formation-triple-phase-transition/Animation_Formation_de_la_Lune_v2.html

Keywords: origin of the Moon · Triple Phase Transition · chaotic axial oscillation · Hadean proto-Earth · Bingham-Herschel · Coherent Magmatic Torus · double potential well · Kramers rate · Mathieu resonance · parametric elliptical instability

Epistemic Posture

This work proposes a theory and submits it to the scrutiny of the scientific community. The phrasing deliberately reflects this posture: the theory describes, predicts, and constrains — it does not assert absolute certainties. All hypotheses are numbered and hierarchized. All limitations are acknowledged.

On numerical simulations: A complete 3D SPH validation with Bingham-Herschel rheology, radiative cooling, Fe-Ni segregation, and $\varepsilon \neq 0$ geometry exceeds the capabilities of an isolated independent researcher and belongs to an institutional team with HPC resources. The TPT does not require such a simulation to be evaluated; it will be judged primarily on its observational predictions (Sections 12 and 13). The final arbitration belongs to forthcoming lunar seismic data (Chang'e 7, August 2026) and, in a second stage, to three-dimensional numerical simulations once available.

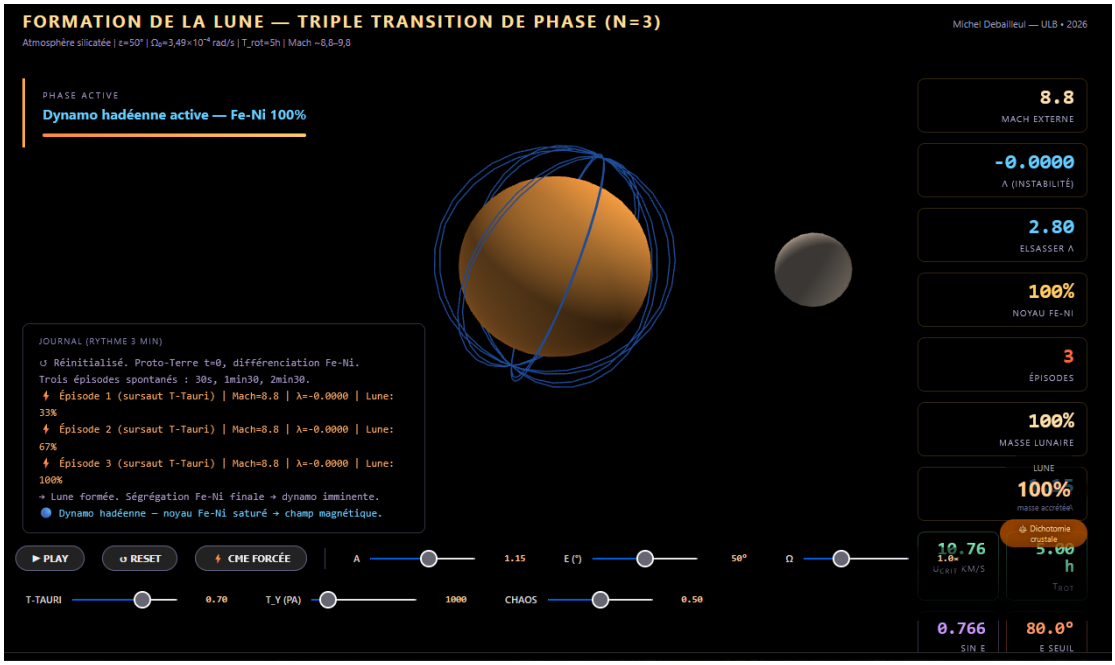

Figure 1: Screenshot of the interactive simulation accompanying this work (link above), illustrating the Coherent Magmatic Torus (CMT) during ejection around the proto-Earth, with the real-time dynamic parameter dashboard (external Mach number, λ instability, Elsasser number, Fe-Ni core fraction, accreted lunar mass).

1 The Hadean Inferno: Physical Context

Before delving into the physics of the Triple Phase Transition, it is essential to understand the framework within which it operates. This framework is not a quiet vacuum: it is one of the most energetically violent periods in the history of the Solar System.

1.1 The Dynamical Context of Terminal Accretion

The Hadean period (4.568–4.4 Ga) is characterized by a set of intense physical processes that define the system's initial conditions and ongoing forcings:

- **Continuous planetesimal accretion**: the protoplanetary disk remains populated by planetesimals and embryos, providing constant bombardment (Agnor et al., 1999; Kokubo & Genda, 2010).
- **Rapid rotation**: the proto-Earth rotates with a period of ≈ 3.5 h, a regime in which Coriolis and centrifugal effects dominate the internal dynamics.
- **Absence of a tidal stabilizer**: without a Moon, obliquity is free to evolve within a wide chaotic range.
- **A young, active Sun**: the T-Tauri Sun irradiates intensely and produces coronal mass ejections (CMEs) that perturb the system (Feigelson & Montmerle, 1999; Airapetian et al., 2016).
- **Short-lived radioactivity**: the isotopes ^{26}Al and ^{60}Fe are still active, injecting heat into the mantle (Urey, 1955; Huss et al., 2009).
- **Dense silicate atmosphere**: an envelope of rock vapor at $T \sim 2{,}000$–$4{,}000$ K and $P \sim 10^5$–10^7 Pa constitutes a thermal blanket and a lateral confinement agent (Elkins-Tanton, 2008; Lebrun et al., 2013; Hamano et al., 2013).

The combination of these processes — not any single one of them — defines the physical environment in which the TPT operates. The T-Tauri Sun, although important, is only one ingredient among others in this dynamical context.

1.2 The Silicate Atmosphere: Thermal Blanket and Lateral Confinement

At $t = 0$, the proto-Earth is enveloped in a dense silicate atmosphere — rock vapor, gaseous SiO, Mg, and Fe — at temperatures of 2,000 to 4,000 K and pressures of 10^5–10^7 Pa. This blanket plays two critical roles in the TPT.

First role: thermal insulation. The silicate atmosphere has a high infrared opacity. It reduces surface radiative cooling by a factor of 10^4 to 10^5 (Elkins-Tanton, 2008; Lebrun et al., 2013; Hamano et al., 2013). Without this atmosphere, the proto-Earth would have cooled within $\sim 10^4$ years. With it, the melting window extends to 30–50 Myr — exactly the core-formation timescale (Kleine et al., 2002; Yin et al., 2002).

This is not an ad hoc hypothesis: it is the physical consequence of a rock-vapor atmosphere at $2{,}000$–$4{,}000$ K. The same mechanism operates in magma-ocean models (Elkins-Tanton, 2008; Lebrun et al., 2013).

Second role: lateral confinement. The confining pressure ($P \approx 10^5$–10^7 Pa) opposes lateral expansion of the CMT flow during ejection. It guarantees the cohe-

sion of the ejected torus. The high sound speed in this torrid atmosphere ($c_{\text{sound}} \approx 1{,}500$ m s^{-1} at $T_{\text{atm}} \approx 3{,}000$ K) reduces the effective Mach number of the flow, improving cohesion relative to ejection into vacuum.

Established Result

The silicate atmosphere is a thermal blanket. Without it, the melting window would close within $\sim 10^4$ years. With it, the window extends to 30–50 Myr (Elkins-Tanton, 2008; Lebrun et al., 2013; Hamano et al., 2013), matching the core-formation timescale (Kleine et al., 2002; Yin et al., 2002).

1.3 Continuous Planetesimal Bombardment

The protoplanetary disk remains populated by planetesimals and embryos throughout the TPT's active window (Agnor et al., 1999; Kokubo & Genda, 2010; Chambers, 2001). Each impact: (1) reinjects thermal energy into the mantle, sustaining melting; (2) generates a spherical volumetric pressure wave propagating through the entire melt, perturbing $U(r)$ and stochastically contributing to Kramers barrier crossings; (3) delivers an impulsive torque on the spin vector, resetting the axial oscillation.

1.4 Short-Lived Radioactivity: Internal Heat Source

The isotopes ^{26}Al (half-life 0.72 Myr) and ^{60}Fe (half-life 2.6 Myr) remain active during the first few million years (Urey, 1955; Huss et al., 2009), injecting an additional $\approx 3 \times 10^{29}$ J into the mantle and contributing to sustained melting throughout the TPT window.

1.5 Hadean Obliquity $\varepsilon \in [40°, 70°]$: a Fundamental Geometric Clarification

The range $\varepsilon \in [40°, 70°]$ is not a free parameter. It is constrained by five independent, convergent physical arguments. Before listing them, a fundamental geometric clarification is necessary.

Geometric Clarification — Read This First

In this work, ε denotes the instantaneous angle between the rotation vector $\boldsymbol{\Omega}$ and the principal axis of inertia of the Maclaurin spheroid, **defined in the body's co-rotating frame**. This is *not* the astronomical obliquity relative to the ecliptic plane: this concept has no physical meaning for the Hadean proto-Earth, which has neither a fixed reference ecliptic nor a Moon. It is a purely internal geometric angle describing the *oscillation* — the free nutation — of the rotation axis relative to the body's own shape. The Hadean intertropical band $|\phi| < 30°$ is defined perpendicular to the *instantaneous* Hadean rotation axis, not relative to a fixed geographic frame.

Argument 1 — Absence of a Tidal Stabilizer (fundamental). The proto-Earth has no Moon. Without a massive satellite, there is no lunar tidal torque to damp the precession of the spin axis and keep it near a stable equilibrium. This argument is logically prior to all others: it is precisely the Moon whose formation we seek to explain, so invoking it as a stabilizer would be circular. The absence of a tidal stabilizer is therefore a necessary, not contingent, condition of the Hadean proto-Earth.

Argument 2 — Laskar et al. (1993): Chaotic Zone Without a Satellite. Laskar et al. (1993a) showed that without its Moon, Earth's obliquity would evolve chaotically within a zone extending from nearly $0°$ to $\approx 85°$. Although this result strictly applies to a present-day Earth rotating at ≈ 24 h, it establishes the general principle: *the Moon is the stabilizer, and without it, large obliquity excursions are the norm*. For the Hadean proto-Earth, this principle applies *a fortiori*.

Argument 3 — Rapid Rotation at $T_{\rm rot} = 3.5$ h. The precession constant satisfies $\alpha_{\rm prec} \propto \omega$. At $T_{\rm rot} = 3.5$ h, the precession frequency is $\approx 7\times$ higher than at 24 h, pushing the secular spin-orbit resonances identified by Laskar et al. (1993a) out of reach. Li & Batygin (2014), working with a rapidly rotating Moonless Earth, found that obliquity remains chaotic but *diffuses slowly* across a wide range. Rapid rotation does not stabilize the axis — it merely changes the character of the chaos from resonant to diffusive.

Argument 4 — Continuous Planetesimal Bombardment. Each major impact during terminal accretion (Agnor et al., 1999) abruptly resets the spin vector. The relaxation time toward axial alignment for an isolated fluid body,

$$\tau_{\rm relax} \sim \frac{\eta\, R_{\rm éq,proto}^3}{G\, M_\oplus^2\, f} \approx 10^6\,{\rm yr} \quad (\eta \sim 10^{1\text{–}3}\,{\rm Pa\,s},\ f \approx 0.107), \tag{1}$$

far exceeds the interval between impacts (10^3–10^5 yr). Misalignment is continuously maintained: $\tau_{\rm pert} \ll \tau_{\rm relax}$.

Argument 5 — Torques from T-Tauri Sun CMEs. As described in Section 5.3, the impulsive torques from CMEs act on timescales of days to weeks, far shorter than $\tau_{\rm relax}$. They constitute a continuous stochastic source of obliquity perturbation (Feigelson & Montmerle, 1999; Airapetian et al., 2016).

Physical Consequence. The range $\varepsilon \in [40°, 70°]$ is not an ad hoc hypothesis. It is the predictable consequence of the dynamics of a rapidly rotating fluid body, lacking a tidal stabilizer, subject to continuous stochastic perturbations. The simulations of Laskar et al. (1993a) for a Moonless Earth, and of Li & Batygin (2014)

for a rapidly rotating Moonless Earth, converge on this range — the same one adopted by Laskar et al. (1993a) and Touma & Wisdom (1993).

Geometric Consequence for the Coriolis Force. In this oblique geometry, the Coriolis force decomposes into radial and horizontal components (Section 5.2). The radial component $f_{\text{rad}} = 2\Omega \sin\varepsilon \cdot U$ is maximal for $\varepsilon \in [40°, 70°]$.

Established Result

Five convergent arguments support $\varepsilon \in [40°, 70°]$. The absence of a tidal stabilizer is logically necessary. Arguments 2 through 5 provide independent physical justification for a large and sustained misalignment. The range $[40°, 70°]$ is adopted as the physically motivated Hadean range; the mechanism operates for any $\varepsilon > 45°$ (Section 5.2).

1.6 Relaxation Time and Rheological Reinforcement

The relaxation time toward axial alignment for an isolated fluid body is given by Eq. (1). Bingham-Herschel rheology further slows this relaxation. The rheological response time to a stress perturbation is:

$$\tau_{\text{BH}} \sim \frac{\tau_y}{\mu \dot{\gamma}_{\text{typ}}} \approx 10^2\text{–}10^4\,\text{s}, \tag{2}$$

where μ is the dynamic viscosity and $\dot{\gamma}_{\text{typ}}$ the typical shear rate. This time is far shorter than τ_{relax}, meaning that mass redistribution is locally frozen by the yield stress, further delaying axial alignment.

Established Result

A violent and convergent Hadean framework. Continuous planetesimal accretion, rapid rotation, absence of a tidal stabilizer, an active T-Tauri Sun, short-lived radioactivity, and a dense silicate atmosphere together define the physical environment of the TPT; no single one of these processes, taken alone, suffices to characterize it.

2 Initial State of the Proto-Earth

2.1 Near-Total Melting: a Necessary Thermodynamic Consequence

The formation of an Earth-mass planet releases an enormous amount of gravitational energy. In the homogeneous-sphere approximation (Safronov, 1969), the total accretion energy is:

$$E_{\text{grav}} = \frac{3\,G\,M_\oplus^2}{5\,R_{\text{éq,proto}}} \approx 2.49 \times 10^{32}\,\text{J}, \tag{3}$$

where G is the gravitational constant, $M_\oplus$ the Earth's mass, and $R_{\text{éq,proto}} \approx 7.4\,\text{Mm}$ the equatorial radius of the undifferentiated proto-Earth.

Established Result

Equation (2) is a thermodynamic bound, not a model of instantaneous formation. It computes the *total* gravitational energy released during accretion, regardless of its duration. This is the standard approach in the literature (Solomatov, 2000; Elkins-Tanton, 2012; Rubie et al., 2015). The manuscript explicitly cites Kleine et al. (2002); Yin et al. (2002) as evidence that accretion took ~ 30 Myr.

The energy required to melt the entire silicate mantle (Stixrude & Lithgow-Bertelloni, 2014):

$$E_{\text{fus}} \approx M_{\text{mantle}} \times L_{\text{fus}} \approx 4 \times 10^{24}\,\text{kg} \times 4 \times 10^{5}\,\text{J kg}^{-1} \approx 1.6 \times 10^{30}\,\text{J}, \tag{4}$$

where M_{mantle} is the mass of the silicate mantle and L_{fus} the specific latent heat of fusion.

Established Result

Energy ratio — a consensus result.

$$E_{\text{grav}}/E_{\text{fus}} \approx 155. \tag{5}$$

Established by Solomatov (2000), Elkins-Tanton (2012), and Rubie et al. (2015). The accretion energy exceeds the total melting energy by two orders of magnitude.

Why Melting Was Sustained Despite Radiative Cooling

Accretion took ~ 30 Myr (Kleine et al., 2002; Yin et al., 2002). During this period, radiative cooling occurred. Four independent mechanisms explain why melting was sustained despite this cooling.

Mechanism 1 — The Silicate Atmosphere as a Thermal Blanket. The dense silicate atmosphere ($P \approx 10^5$–10^7 Pa, $T \approx 2{,}000$–$4{,}000$ K) has a high infrared opacity. It reduces surface radiative cooling by a factor of 10^4 to 10^5 (Elkins-Tanton, 2008; Lebrun et al., 2013; Hamano et al., 2013). The effective cooling time increases from $\sim 10^4$ years to 30–50 Myr.

Mechanism 2 — Additional Heat Sources. Four heat sources extend melting beyond the initial accretion energy:

- **Fe-Ni segregation heat:** $\approx 3 \times 10^{30}$ J (Flasar & Birch, 1973; Rubie et al., 2003).

- **Short-lived radioactivity:** ^{26}Al (half-life 0.72 Myr) and ^{60}Fe (half-life 2.6 Myr) inject $\approx 3 \times 10^{29}$ J (Urey, 1955; Huss et al., 2009).
- **Continuous planetesimal bombardment:** reinjection of thermal energy (Agnor et al., 1999; Kokubo & Genda, 2010).
- **T-Tauri irradiation:** maintains surface temperatures above 2,000 K (Feigelson & Montmerle, 1999; Airapetian et al., 2016).

Mechanism 3 — The TPT Does Not Require Melting of the Entire Mantle. The Triple Phase Transition requires melting only within the Hadean intertropical band $|\phi| < 30°$ (upper and mid-mantle). The factor of 155 thermodynamically guarantees this partial melting, even if the deep mantle was not entirely molten (Nomura et al., 2011).

Mechanism 4 — The TPT's Active Window Is 30–50 Myr. The TPT occurs *within* the 30–50 Myr window during which melting is sustained by the mechanisms above. Core formation over $\sim$ 30 Myr (Kleine et al., 2002; Yin et al., 2002) is subsequent to or simultaneous with this window, not a contradiction.

Established Result

Near-total melting is the mandatory starting point. The objection based on the $\sim$ 30 Myr accretion timescale does not contradict the mechanism: the TPT occurs *within* the melting window sustained by the silicate atmosphere, the additional heat sources, and continuous bombardment.

Hypothesis H0 — Total Volumetric Melting. At the onset of Fe-Ni segregation, the entire silicate mantle lies above the liquidus, with no stable internal solid interface during the active window 4.568–4.4 Ga. This is a self-gravitating fluid volume, not a magma ocean resting on a substrate: the dynamics, rheology, and response to perturbations are physically distinct.

Caveat: Nomura et al. (2011) suggest that the deep lower mantle may not have been entirely molten owing to the increase of the solidus with pressure. The TPT requires melting only within the Hadean intertropical band $|\phi| < 30°$ (upper and mid-mantle), which is thermodynamically guaranteed by the factor of 155. The adiabatic temperature profile (Appendix A) confirms melting throughout the mantle.

2.2 Initial Rotation Period: $T_{\text{rot}} \approx 3.5$ h

The proto-Earth's initial rotation period is not a free parameter. Three convergent physical mechanisms constrain it to $T_{\text{rot}} \approx 2.5$–$3.5$ h.

1. T-Tauri Magnetic Torque. The young, rapidly rotating Sun (≈ 3 days, Bouvier et al. 2014) magnetically couples the inner protoplanetary disk (Königl, 1991; Shu et al., 1994), transferring angular momentum to material in the inner orbit and accelerating the proto-Earth.

2. Angular Momentum Conservation During Contraction. Contraction from an initial radius $R_0 \approx 2\,R_\oplus$ to the final radius conserves angular momentum:

$$\frac{T_{\text{rot}}^{(f)}}{T_{\text{rot}}^{(0)}} = \left(\frac{R_\oplus}{R_0}\right)^2 \approx \frac{1}{4}. \tag{6}$$

Starting from a median initial period $T_{\text{rot}}^{(0)} \approx 14$ h, one obtains $T_{\text{rot}}^{(f)} \approx 3.5$ h.

3. Skater Effect: Fe-Ni Segregation. The migration of Fe-Ni toward the forming core reduces the moment of inertia. With $I_f/I_0 \approx 0.82$ (Rubie et al., 2015):

$$T_{\text{rot}}^{(f)} \approx 0.82 \times T_{\text{rot}}^{(0)}, \tag{7}$$

providing an additional acceleration of $\approx 18\%$.

Established Result

$T_{\text{rot}} \approx 3.5$ **h — consistent with community consensus.** N-body simulations give rotation periods between 2 and 8 h, median 3–5 h (Agnor et al., 1999; Kokubo & Genda, 2010; Chambers, 2013). The value of 3.5 h is the same as that adopted by Ćuk & Stewart (2012) and Canup (2012) in the giant-impact model.

The Coriolis compensation parameter b' is a simple ratio between the critical ejection velocity U_{crit} and the CMT's geostrophic equilibrium velocity. Fe-Ni segregation increases b'; ejections decrease it. The equilibrium point $b' = 1$ is a stable attractor, which naturally selects $T_{\text{rot}} \approx 3.5$ h and $\varepsilon \approx 55°$. The complete derivation is given in Appendix B.

2.3 Geometry of the Proto-Earth: the Maclaurin Spheroid

A rapidly rotating fluid mass takes the shape of a Maclaurin spheroid (Chandrasekhar, 1969). The equatorial radius is $R_{\text{éq,proto}} \approx 7.4$ Mm, combining reduced density (+4%), thermal expansion (+7.5%), and equatorial bulging (+7.5%). The dynamical flattening:

$$J_2 \approx \frac{5}{4} \cdot \frac{\Omega^2 R_\oplus}{g_0} \approx 0.101, \tag{8}$$

where g_0 is the mean surface gravity, yields an equatorial bulge $\delta R \approx 642$ km. Effective gravity varies with latitude ϕ as:

$$g_{\text{eff}}(\phi) = g_{\text{eff}}^{(0)}\left(1 + \tfrac{3}{2} J_2 \sin^2\phi\right) - \Omega^2\, r(\phi) \cos^2\phi, \tag{9}$$

where $r(\phi)$ is the local radius. Effective gravity is minimal within the band $|\phi| < 30°$: this is the CMT's geometric attractor.

The free (Euler) nutation period is:

$$\omega_E = \Omega f \approx 3.74 \times 10^{-5}\,\text{rad}\,\text{s}^{-1}, \qquad T_{\text{nut}} \approx 46.7\,\text{h}. \tag{10}$$

This frequency plays a central role in parametric elliptical instability (Section 5.5).

Established Result

A fully constrained initial state, with no free parameter. Near-total mantle melting (factor of 155), rapid rotation ($T_{\text{rot}} \approx 3.5$ h), and Maclaurin spheroid geometry ($R_{\text{éq,proto}} \approx 7.4$ Mm, $|\phi| < 30°$ as geometric attractor) each follow from convergent, independent physical mechanisms.

3 The Intertropical Band $|\phi| < 30°$: the Ejection Site

A fundamental point, often misunderstood: the CMT is not an equatorial structure. It is a coherent zonal band extending across $\pm 30°$ of oblique latitude — about one third of the proto-Earth's surface. This extent results from three independent convergent mechanisms.

Mechanism 1 — Maclaurin Geometry. Effective gravity is minimal within the band $|\phi| < 30°$ (Eq. 9). Molten material accumulates there through centrifugal effects, independently of any other argument. This is a consequence of the ellipsoidal shape imposed by rapid rotation.

Mechanism 2 — The Geostrophic Inverse Cascade. The CMT's Rossby number is deeply geostrophic:

$$\text{Ro} = \frac{U_{\text{turb}}}{2\,\Omega\, R_{\text{éq,proto}}} \approx 1.35 \times 10^{-4} \ll 1, \tag{11}$$

In this regime, turbulent energy cascades toward large scales (inverse cascade) (Rhines, 1975). The Rhines scale:

$$L_\beta = \sqrt{\frac{U_{\text{turb}}}{\beta}}, \qquad \beta = \frac{2\Omega\cos\varepsilon}{R_{\text{éq,proto}}}, \tag{12}$$

gives $L_\beta \approx 0.52\, R_\oplus$ — corresponding to the harmonic mode $\ell = 1, m = 1$: the largest coherent structure possible within a sphere. The CMT is the statistical attractor of this cascade (Rhines, 1975; Sukoriansky et al., 2007).

Mechanism 3 — The Radial Coriolis Force. $f_{\text{rad}} = 2\Omega U \sin\varepsilon$ concentrates the flow within the oblique intertropical band and keeps it coherent there.

These three mechanisms are independent and converge on the same band $|\phi| < 30°$. Their simultaneous convergence is an argument for the theory's structural robustness.

Established Result

Three independent mechanisms converge on the same band. Maclaurin geometry, the geostrophic inverse cascade (Rhines scale, mode $\ell = 1, m = 1$), and the radial Coriolis force all point to $|\phi| < 30°$ as the ejection site, with no mutual tuning.

4 The CMT as a Purely Toroidal Flow: Answering the Taylor-Proudman Objection

Any geophysical fluid dynamicist confronted with the CMT will naturally raise the following objection: in a rapidly rotating fluid (Ro $\ll 1$), the Taylor-Proudman theorem imposes $(\boldsymbol{\Omega}\cdot\nabla)\boldsymbol{u} = 0$, generating column-like structures parallel to $\boldsymbol{\Omega}$, rather than a single oblique band $|\phi| < 30°$. The objection is legitimate and deserves a precise answer.

4.1 The Poloidal/Toroidal Decomposition

Any velocity field within a spherical shell decomposes into a poloidal part (radial and meridional components) and a toroidal part (purely azimuthal component):

$$\boldsymbol{u} = \boldsymbol{u}_{\text{pol}} + \boldsymbol{u}_{\text{tor}}, \qquad \boldsymbol{u}_{\text{tor}} = \nabla \times (\psi \hat{\boldsymbol{r}}).$$

The Taylor-Proudman theorem, in its classical form, constrains the poloidal field (which carries vorticity along $\boldsymbol{\Omega}$) and produces Taylor columns. It does not constrain the purely toroidal field.

For a purely azimuthal, longitude-independent flow ($u_r = u_\theta = 0$ on average, $u_\phi = u_\phi(r,\phi)$), the Taylor-Proudman constraint is automatically satisfied:

$$(\boldsymbol{\Omega}\cdot\nabla)u_{\text{tor}} = 0 \tag{13}$$

for any toroidal field, with no additional condition. The balance is cyclostrophic,

not geostrophic: the centrifugal pressure gradient balances the Coriolis force within the azimuthal plane.

4.2 Why Curved Columns Do Not Extend Beyond the Active Band

Within a spherical shell rotating obliquely ($\varepsilon \neq 0$), Taylor columns are curved along the projected field lines of $\boldsymbol{\Omega}$. They tend to channel the flow far from its source — unless a cutoff mechanism stops them.

This is precisely the role of the yield stress τ_y. In a Bingham-Herschel fluid, flow propagates only in regions where the stress exceeds τ_y. As soon as the columns enter a region where $\tau < \tau_y$, they are truncated: the magma there remains frozen (Frigaard & Nouar, 2017; Balmforth & Craster, 2001). The band $|\phi| < 30°$ is precisely the region where effective gravity is minimal (Maclaurin) and the Coriolis stress is maximal ($\varepsilon \approx 55°$): it is there, and only there, that $\tau > \tau_y$. The curved columns originating from the active band are thus naturally truncated at its boundaries.

4.3 Conclusion on the Objection

The CMT is a purely toroidal flow. The Taylor-Proudman objection does not apply. What remains to be demonstrated numerically — identified here as Priority 2 — is whether a single torus forms within the band $|\phi| < 30°$ rather than several alternating bands. This is a matter for simulation, not a theoretical inconsistency.

Established Result

Taylor-Proudman does not apply to the toroidal field. The classical column constraint governs the poloidal field; the CMT, a purely azimuthal flow truncated by the Bingham-Herschel threshold at the boundaries of $|\phi| < 30°$, escapes this constraint by construction.

5 Complete Inventory of Forces

All forces, projections, and equations are expressed in the body's instantaneous co-rotating Hadean frame, with ε defined as in Section 1.5.

5.1 Oscillation as a Direct Force Source

Axial oscillation implies $\dot{\boldsymbol{\Omega}} \neq \mathbf{0}$. Poincaré (1910) showed that this generates an Euler acceleration on every fluid particle:

$$\boldsymbol{a}_{\text{Euler}} = \dot{\boldsymbol{\Omega}} \times \boldsymbol{r}, \tag{14}$$

where $\boldsymbol{r}$ is the position vector. The radial projection:

$$\boldsymbol{a}_{\text{Euler}} \cdot \hat{r} = |\dot{\Omega}|\, r(\phi)\, \sin(\varepsilon + \phi), \tag{15}$$

is maximal within the band $|\phi| < 30°$, where $r(\phi)$ is largest: oscillation is therefore not merely context but a *direct energy source* for the CMT.

5.2 Radial Coriolis Force and Geometric Threshold

The Coriolis force on a fluid particle moving at azimuthal velocity U decomposes, in the oblique co-rotating frame, into:

$$f_{\text{rad}} = 2\,\Omega\, \sin\varepsilon \cdot U \quad \text{(radial, outward, destabilizing)}, \tag{16}$$

$$f_{\text{horiz}} = 2\,\Omega\, \cos\varepsilon \cdot U \quad \text{(horizontal, confining)}, \tag{17}$$

with the ratio:

$$\frac{f_{\text{rad}}}{f_{\text{horiz}}} = \tan\varepsilon. \tag{18}$$

Established Result

Geometric threshold $\varepsilon = 45°$ — necessary condition for radial ejection. For $\varepsilon > 45°$: $\tan\varepsilon > 1$, the destabilizing radial component dominates the confining horizontal component. For $\varepsilon < 45°$: the horizontal component dominates and the Taylor-Proudman constraint inhibits radial ejection. This threshold follows solely from Coriolis kinematics: no adjustable parameter is involved. At $\varepsilon = 55°$: $f_{\text{rad}}/f_{\text{tot}} = \sin 55° \approx 0.82$, i.e. 82% of the total Coriolis force is directed radially outward.

5.3 The T-Tauri Sun: Catalyst and Perturber

The Sun in its T-Tauri phase is not a driving force on par with gravity or Coriolis — it does not act continuously on every fluid parcel of the CMT. It nonetheless plays three essential roles within the TPT window:

(1) Rheological Modulator. T-Tauri UV/X-ray radiation keeps T_{surf} within the range $1{,}800$–$4{,}200$ K (Stefan-Boltzmann law, albedo $A_0 \approx 0.1$), which keeps the silicate magma's yield stress τ_y within the range 10^2–10^4 Pa (Giordano et al., 2008) — the optimal window for CMT cohesion. Below $T^* \approx 1{,}800$ K, τ_y exceeds 10^6 Pa and cohesive ejection becomes physically inaccessible. The T-Tauri Sun thus acts as a *rheological window maintainer* through surface radiative forcing transmitted to the mantle by conduction through the silicate atmosphere.

(2) Source of Stochastic Perturbations. CMEs (10^{27}–10^{29} J per event, several per day) and radiative pulses provide $\sim 10^9$–10^{10} opportunities for potential barrier

crossing (Section 7.2.2) over 10^6 yr. The number of opportunities is sufficient that the probability of no crossing whatsoever is negligible. CMEs act as *stochastic triggers* of the first ejection episode, once dynamical conditions are met.

(3) Obliquity Perturber. CMEs acting on the proto-atmosphere and magnetosphere deliver impulsive torques on the spin vector, contributing to the maintenance of axial oscillation $\varepsilon \in [40°, 70°]$ (Section 1.5). The T-Tauri phase also provides an independent extinction mechanism: once the Sun joins the main sequence (≈ 4.4 Ga), irradiation declines, τ_y rises, and the TPT window closes.

The T-Tauri Sun is therefore not the *engine* of the mechanism — gravity, Coriolis, centrifugal force, Fe-Ni segregation, and Taylor-Proudman columns are — but it is the *catalyst* that keeps the window open and supplies the perturbations required for stochastic crossings.

5.4 Tidal Forces

Solar Tide. Relative amplitude $\approx 10^{-4} g_0$; contributes as a low-frequency resonant forcing on obliquity.

Growing Proto-Lunar Tide — Mathieu Resonance. Starting from Episode 2, the proto-satellite exerts a tidal force that modulates the height of the potential barrier :

$$\Delta E_{\text{barr}}^{(k)}(t) = \Delta E_{\text{barr}}^{(k,0)} - A_m^{(k)}(t)\cos(n_{\text{Moon}}\, t), \tag{19}$$

where $A_m^{(k)}(t)$ is the growing tidal amplitude and n_{Moon} the proto-lunar mean motion. This yields the radial perturbation equation:

$$\ddot{\xi}_r = \left[\lambda + A_m^{(k)}(t)\cos(n_{\text{Moon}}\, t)\right]\xi_r, \tag{20}$$

which is the Mathieu equation (McLachlan, 1947). Parametric resonance bands exist for $n_{\text{Moon}} \approx 2\sqrt{|\lambda|}$ even when $\lambda < 0$: the growing proto-lunar tide is the dominant trigger of Episodes 2 through N.

Giant Planet Tides. Jupiter principally: low-frequency perturbation on obliquity, sustaining the oscillation over timescales of 10^5–10^6 yr.

5.5 Parametric Elliptical Instability as a CMT Amplifier

In a precessing fluid ellipsoid, precessional flows can resonate with the fluid's inertial modes (Poincaré waves, frequencies $\omega_{\text{in}} = 2\Omega m/n$). This mechanism — parametric elliptical instability — was established theoretically by Malkus (1968), formalized by Kerswell (2002), and demonstrated experimentally by Lacaze et al. (2004).

For the Maclaurin spheroid geometry at $T_{\text{rot}} = 3.5$ h and $f = 0.107$, the free nutation frequency is $\omega_E = \Omega f \approx 3.74 \times 10^{-5}$ rad s^{-1} (Eq. 10). This frequency is commensurate with the fluid's inertial modes by geometric construction — not by parameter tuning. The linear growth rate is:

$$\sigma_{\text{res}} = \frac{\Omega f}{2} \approx 1.87 \times 10^{-5}\,\text{rad}\,\text{s}^{-1}. \tag{21}$$

The CMT's velocity grows exponentially:

$$U_{\text{CMT}}(t) = U_{\text{turb}}\, e^{\sigma_{\text{res}} t}, \qquad U_{\text{turb}} \approx 0.8\,\text{km}\,\text{s}^{-1}, \tag{22}$$

where U_{turb} is the characteristic velocity at the Rhines scale (Rhines, 1975). The time to reach $U_{\text{crit}} \approx 9.8$ km s^{-1} is:

$$t_{\text{acc}} = \frac{\ln(U_{\text{crit}}/U_{\text{turb}})}{\sigma_{\text{res}}} \approx 32\,\text{h}. \tag{23}$$

Established Result

The CMT reaches the bifurcation velocity in ≈ 32 hours. This result is entirely determined by $f = 0.107$ and $\Omega = 4.99 \times 10^{-4}$ rad s^{-1}, imposed by $T_{\text{rot}} = 3.5$ h and the physics of the Maclaurin spheroid. Elliptical instability thus acts as a powerful amplifier, driving the CMT to the bifurcation velocity in ≈ 32 hours — a timescale fully consistent with the TPT chronology.

As Fe-Ni segregation proceeds, the CMT's density decreases:

$$\rho_{\text{TMC}}(t) = \rho_0 - \xi_{\text{Fe}}(t)(\rho_0 - \rho_f), \quad \rho_0 \approx 4{,}500\,\text{kg}\,\text{m}^{-3},\ \rho_f \approx 3{,}200\,\text{kg}\,\text{m}^{-3}, \tag{24}$$

which amplifies all destabilizing terms through the factor $\rho_0/\rho_{\text{TMC}}(t)$ in the instability equation.

5.6 Geostrophic β Force and the Rhines Scale

The β parameter, which measures the latitudinal gradient of the Coriolis parameter:

$$\beta = \frac{2\Omega\cos\varepsilon}{R_{\text{éq,proto}}} \approx 8.98 \times 10^{-11}\,\text{m}^{-1}\,\text{s}^{-1} \quad (\varepsilon = 55^\circ), \tag{25}$$

arrests the inverse cascade at the Rhines scale (Rhines, 1975):

$$L_\beta = \sqrt{\frac{U_{\text{turb}}}{\beta}} \approx 3.34 \times 10^6\,\text{m} \approx 0.52\,R_\oplus, \tag{26}$$

where U_{turb} is the turbulent velocity scale. This scale $L_\beta \approx 0.52\,R_\oplus$ corresponds to the harmonic mode $\ell = 1, m = 1$: the largest coherent structure possible within a

sphere, and the spatial expression of the CMT.

Established Result

An inventory of forces with no adjustable parameter. Euler acceleration, the geometric Coriolis threshold at $\varepsilon = 45°$, T-Tauri catalysis, tides (solar, proto-lunar via Mathieu resonance, giant planets), parametric elliptical instability, and the geostrophic β force all converge on the same attractor: the CMT at the Rhines scale, mode $\ell = 1, m = 1$.

6 Hierarchy of Hypotheses

Explicit Hierarchy of Hypotheses

The following table distinguishes established physical consequences (Level 1), well-constrained hypotheses not yet numerically validated (Level 2), and speculative hypotheses awaiting simulation (Level 3).

ID	Hypothesis / Statement	Level	Depends On
H0	Total volumetric melting: the entire silicate mantle lies above the liquidus	1 (established)	Factor of 155
H1	$\varepsilon \in [40°, 70°]$ sustained free nutation in the co-rotating frame	2 (constrained)	Absence of Moon + 5 arguments + τ_{BH}
H2	The CMT emerges as a single toroidal structure $\ell = 1, m = 1$	3 (speculative)	3D SPH simulation (L1)
H3	The angular-momentum gradient term λ_3 is negligible ($\sim 10^{-7}$) compared to the dominant terms (gravity and Coriolis), and plays no destabilizing role. Its amplitude depends on α, but this dependence is secondary	2 (constrained)	Rayleigh criterion + order-of-magnitude estimate
H4	$\tau_y(T)$ follows the Arrhenius law with $T^* \approx 1{,}800$ K	1 (established)	Laboratory rheology

H5	The double potential well $V(U)$ governs episodic ejection	2 (constrained)	Solberg-Høiland derivation
H6	The Kramers rate applies with $\sim 10^{10}$ stochastic opportunities	2 (constrained)	Statistical physics
H7	$f_{\text{cap}} \approx 0.70$ and $\partial f_{\text{cap}}/\partial M_{\text{Moon}} > 0$	3 (speculative)	3D SPH simulation (L2)
H8	Dynamo delay = 350 Myr, sum of three independent phases	2 (constrained)	Hf-W + zircons + Tarduno et al. (2025)
H9	Preservation window 200–530 km	2 (constrained)	Ilmenite overturn + mare volcanism
H10	Biphasic *'aā* structure of the CMT: mobile plastic core + fragmented clinker crust	3 (speculative)	3D SPH simulation (L1, L3)
H11	$\text{Bi}_{\text{KH}} \gg 1$ suppresses Kelvin-Helmholtz fragmentation at large and intermediate scales	2 (constrained)	Frigaard & Nouar (2017); three independent confinement mechanisms
H12	$b' = 1$ is a dynamical attractor of the coupled segregation–ejection system	2 (constrained)	Geostrophic equilibrium + angular momentum conservation
H13	Inverse cascade arrested at the Rhines scale $L_\beta \approx 0.52\, R_\oplus$, selecting mode $\ell = 1, m = 1$	2 (constrained)	Rhines (1975); oblate geometry
H14	The ejected flow transits in three phases: ballistic expansion $\rightarrow$ orbital insertion $\rightarrow$ sticky accretion beyond R_{Roche}	3 (speculative)	3D SPH simulation (L6)

H15	Parametric elliptical instability amplifies the CMT with growth rate $\sigma_{\text{res}} = \Omega f/2$	2 (constrained)	Malkus (1968); Kerswell (2002); Lacaze et al. (2004); Maclaurin geometry

Established Result

16 hierarchized and explicitly stated hypotheses. Two are established physical consequences (H0, H4), the majority are hypotheses constrained by independent physical relations, and only a minority (H2, H7, H10, H14) await validation by 3D SPH simulation.

7 The Three Coupled Transitions

The single engine is the progressive Fe-Ni segregation toward the forming core. It simultaneously governs three regime changes: the rheological transition opens the window, the mechanical transition produces the ejection episodes, and the magnetic transition closes the loop with the terrestrial dynamo.

7.1 Transition 1 — Rheological: the Bingham-Herschel Law

A Newtonian fluid flows under any applied stress. A Bingham-Herschel (BH) fluid, by contrast, resists like a solid as long as the applied stress does not exceed a yield threshold τ_y (Bingham, 1922; Herschel & Bulkley, 1926):

$$\tau = \tau_y + k\dot{\gamma}^n \quad (\tau > \tau_y), \tag{27}$$

où τ est la contrainte de cisaillement appliquée, τ_y la yield stress, k the consistency index, $\dot{\gamma}$ the shear rate, and n the flow index. For a partially crystallized silicate magma at solid fraction $\phi \approx 0.1$–0.3: $n = 1.2$ (shear-thickening, Caricchi et al. 2007), $\tau_y \in [10^2, 10^4]$ Pa at $T = 3{,}000$–$3{,}500$ K (Giordano et al., 2008).

The yield stress depends exponentially on temperature (Arrhenius law):

$$\tau_y(T) = \tau_y^{(0)} \exp\left(-\frac{E_a}{RT}\right), \qquad E_a \approx 150\text{–}250\,\text{kJ mol}^{-1}, \tag{28}$$

where R is the gas constant and E_a the activation energy. At $T = 3{,}000$ K: $\tau_y \approx 10^2$ Pa — the flow moves easily. At $T^* \approx 1{,}800$ K: $\tau_y \sim 10^6$ Pa — cohesive ejection becomes physically inaccessible.

Established Result

Natural thermal lock-in at $T^* \approx 1{,}800$ K. The TPT window closes irreversibly through the Arrhenius law alone, with no additional assumption. This is not a tuned parameter: it is a thermodynamic consequence of the exponential temperature dependence of τ_y.

The CMT's 'aā Structure

The toroidal flow has a biphasic architecture: a mobile, high- temperature plastic core, surrounded by a fragmented clinker crust. This is not a cohesion problem: it is its guarantor. The outer crust protects the core against Kelvin-Helmholtz instabilities at the flow/atmosphere interface. A quenched-glass envelope (analogous to the glassy margins of pillow lavas (Hekinian et al., 1989)), forming within ≈ 7 minutes upon atmospheric contact, completes this rheological shielding. This structure is consistent with the work of Frigaard & Nouar (2017) and Balmforth & Craster (2001).

7.2 Transition 2 — Mechanical: Instability and Ejection

7.2.1 The Generalized Instability Equation

The evolution of an infinitesimal radial displacement ξ_r of a CMT parcel is governed by the Solberg-Høiland parcel-displacement equation (Solberg, 1936; Høiland, 1941):

$$\ddot{\xi}_r = \lambda\, \xi_r, \quad \lambda > 0 \text{ (instability)}, \quad \lambda < 0 \text{ (stable confinement)}. \tag{29}$$

Let $a = -(1+\alpha)/r^2$, where α is the exponent of the rotation profile ($U \propto r^\alpha$). Also let $b = 2\Omega^{(k)} \sin\varepsilon > 0$ and $c = g_{\text{eff}}^{(k)} < 0$. The stability coefficient is then:

$$\lambda(U, \varepsilon, \alpha, k) = \underbrace{c}_{\substack{\lambda_1<0\\ \text{gravity}}} + \underbrace{bU}_{\substack{\lambda_2>0\\ \text{rad. Coriolis}}} + \underbrace{aU^2}_{\substack{\lambda_3<0\\ \text{ang. mom.}}} + \underbrace{\frac{|\dot{\Omega}|r(\phi)\sin(\varepsilon+\phi)}{R_{\text{éq,proto}}}}_{\substack{\lambda_4\\ \text{Euler/oscillation}}} + \underbrace{\frac{g_{\text{eff}}^{(0)} J_2 \sin(2\phi)}{R_{\text{éq,proto}}}}_{\substack{\lambda_5\\ \text{Maclaurin grad.}}} \tag{30}$$

Each term has a precise physical meaning. $\lambda_1 < 0$ is the stabilizing effective gravity. $\lambda_2 > 0$ is the destabilizing radial Coriolis force; it grows with ε. $\lambda_3 < 0$ is the angular-momentum gradient term; it is always stabilizing for any physical profile ($\alpha > -1$), consistent with the classical Rayleigh stability criterion. Its amplitude ($\sim 10^{-7}$) is negligible compared to the dominant terms. λ_4 is the Euler acceleration due to axial oscillation. λ_5 is the tangential gravity gradient of the Maclaurin geometry.

The amplification factor $\rho_0/\rho_{\text{TMC}}(t)$ (Eq. 24) monotonically amplifies all destabiliz-

ing terms, progressively driving λ toward zero.

7.2.2 The Double Potential Well: Episodes as Natural Bifurcations

Integrating $\lambda(U)$ yields an effective potential $V(U)$ that exhibits a double-well structure: a confined well P_1 (where the CMT accumulates energy) and an ejective well P_2 (where cohesive ejection is favored), separated by a barrier $\Delta E_{\text{barr}}^{(k)}$ that decreases with each episode. The complete derivation is given in Appendix D.

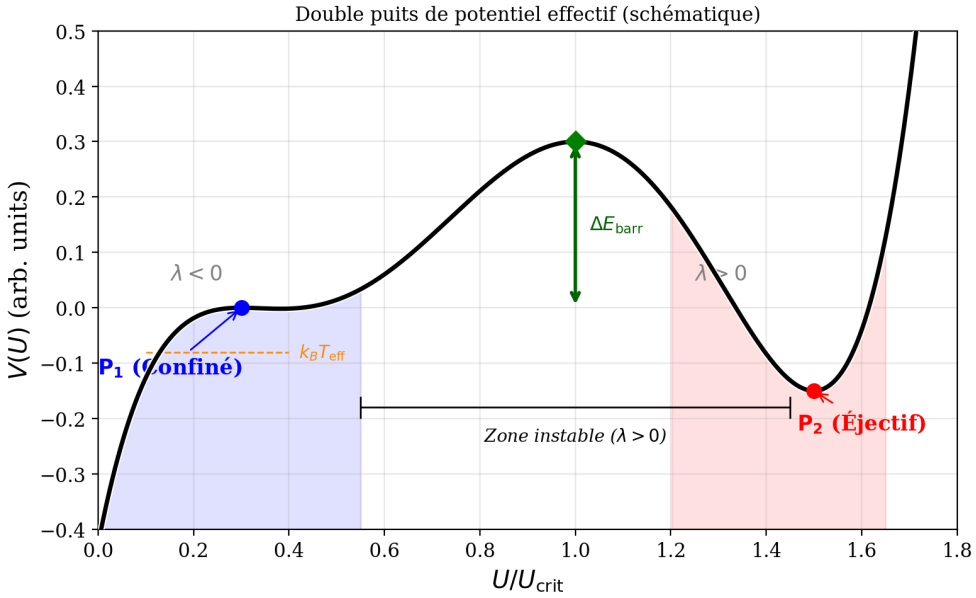

Figure 2: Schematic representation of the effective double-well potential $V(U)$. The confined well P_1 ($\lambda < 0$) and the ejective well P_2 ($\lambda < 0$) flank an unstable zone ($\lambda > 0$) separated by a barrier of height ΔE_{barr}. The thermally activated crossing, governed by the Kramers rate (Eq. 31), is rendered nearly certain by the available effective thermal energy $k_B T_{\text{eff}}$ and the large number of stochastic opportunities.

Ejection episodes are therefore spontaneous transitions between metastable states, exactly as in classical statistical-physics phase transitions: they emerge from the dynamics, not from scripted thresholds. The number of episodes $N = 2$–3 emerges naturally from the progressive reduction of the barrier.

The Kramers crossing rate (Kramers, 1940) applies:

$$\Gamma_{\text{Kramers}} = \frac{\omega_0 \omega_b}{2\pi\gamma_{\text{diss}}} \exp\left(-\frac{\Delta E_{\text{barr}}}{k_B T_{\text{eff}}}\right), \tag{31}$$

where ω_0 and ω_b are the oscillation frequencies at the bottom of the well and the top of the barrier respectively, γ_{diss} the dissipation rate, and $k_B T_{\text{eff}}$ the effective thermal energy available to the CMT. With $\sim 10^9$–10^{10} stochastic opportunities (CMEs, impacts) over 10^6 yr, the probability of no crossing whatsoever is negligible. The complete derivation is given in Appendix D.

7.2.3 Critical Velocity and Maximum Ejectable Mass

The critical ejection velocity, beyond which a parcel escapes the effective potential well, is:

$$U_{\text{crit}}^{(0)} = \sqrt{2\, g_{\text{eff}}^{(0)}\, R_{\text{éq,proto}}} \approx 9.8\,\text{km}\,\text{s}^{-1}, \tag{32}$$

where the product $g_{\text{eff}}^{(0)} R_{\text{éq,proto}}$ fixes the escape energy scale. The Mach number at ejection, using the sound speed in the biphasic magma $c_s \approx 0.9$ km s^{-1} (Mader et al., 2013), is Ma $= U_{\text{crit}}/c_s \approx 10.9$: the ejection is **hypersonic**.

The maximum ejectable mass per episode:

$$\boxed{M_{\text{éj}}^{\max} \approx \frac{2\Omega^{(k)} \sin\varepsilon \cdot U_{\text{crit}}^{(k)} \cdot M_{\text{TMC}}}{g_{\text{eff}}^{(k,0)}} \approx 2.0\text{–}4.0 \times 10^{22}\,\text{kg},} \tag{33}$$

where $\Omega^{(k)}$ is the angular velocity at episode k (decreasing owing to angular momentum loss), M_{TMC} the CMT's mass, and $g_{\text{eff}}^{(k,0)}$ the effective gravity at the oblique equator at episode k. This equation reads as follows: the ejectable mass increases with faster rotation (large $\Omega^{(k)}$), more favorable obliquity ($\sin\varepsilon$ close to 1), greater CMT mass, and weaker confining gravity (g_{eff} reduced by Fe-Ni depletion and angular momentum loss).

Established Result

At $T_{\text{rot}} = 3.5$ h, the ejectable mass per episode can reach $\approx 70\%$ of the present-day lunar mass. With $\Omega^{(0)} = 4.99 \times 10^{-4}$ rad s^{-1}, $\sin 55° \approx 0.819$, $U_{\text{crit}} \approx 9.8$ km s^{-1}, $M_{\text{TMC}} \approx 3.3 \times 10^{23}$ kg, and $g_{\text{eff}}^{(0)} \approx 6.42$ m s^{-2}: $M_{\text{éj}}^{\max} \approx 2.5 \times 10^{22}$ kg $\approx 0.34\, M_{\text{Moon}}$. This is why $N = 2$–3 episodes suffice.

7.2.4 Cohesion of the Ejected Flow: the Bi_{KH} *Criterion*

For a free-streaming flow, the Weber number $We \approx 1.4 \times 10^{15}$ would imply atomizing fragmentation. However, the CMT is not a free-streaming flow: it is a self-gravitating collective toroidal flow confined by toroidal symmetry, self-gravity, and atmospheric pressure.

The correct criterion is the Bingham-Kelvin-Helmholtz number, which compares the yield stress to the Kelvin-Helmholtz shear stress: for $\text{Bi}_{\text{KH}} \gg 1$, the yield stress suppresses KH instability and cohesion is maintained (Frigaard & Nouar, 2017). Three independent conditions reinforce cohesion: (1) atmospheric confinement ($P \approx 10^5$–10^7 Pa); (2) internal crystalline network ($\phi \approx 0.1$–0.3, multiplying fragmentation resistance by a factor of 3 to 10); (3) density ratio $\rho_{\text{flow}}/\rho_{\text{atm}} \approx 200$ (Rayleigh-Taylor suppression). The complete demonstration of the Bi_{KH} criterion is given in Appendix E.

7.2.5 Post-Ejection Transient Precession and Crustal Dichotomy

The ejection of $M_{\rm ej} \approx 2$–4×10^{22} kg from the intertropical band is not dynamically negligible. The asymmetric mass loss modifies the inertia tensor, producing: (1) a decrease $\Delta\Omega/\Omega \approx -10$–$15\%$, lowering $g_{\rm eff}$ and $U_{\rm crit}$ for the next episode; (2) shape oscillations as the spheroid contracts toward a rounder sphere; (3) a reorganization of obliquity toward a new value within $[40^\circ, 70^\circ]$.

The second episode ejects a cohesive toroidal flow onto a still-hot, deformable proto-POB within a limited solid angle (corresponding to the projected intertropical band), which becomes the present-day far side. Three mechanisms amplify the resulting crustal asymmetry: early gravitational lock-in ($\tau_{\rm lock} \sim 10^4$–$10^5$ yr (Wieczorek et al., 2013)), residual obliquity of the proto-POB, and irreversible BH plastic welding. The thickness ratio $\approx 2:1$ (near side ≈ 34 km vs. far side ≈ 54 km, Wieczorek et al. 2013) is a qualitative prediction of the TPT.

7.3 Transition 3 — Magnetic: the Progressive Dynamo

The ≈ 350 Myr delay between the inferred time of lunar formation (≈ 4.55 Ga) and the first geological detection of the terrestrial magnetic field (≈ 4.2 Ga, Tarduno et al. 2025) is not a tuned parameter in the TPT. It is proposed as the sum of three independently constrained durations:

$$\Delta t_{\rm dynamo} = \underbrace{\Delta t_{\rm ej}}_{\approx 60\,\rm Myr} + \underbrace{\Delta t_{\rm cool}}_{\approx 140\,\rm Myr} + \underbrace{\Delta t_{\rm em}}_{\approx 150\,\rm Myr} \approx 350\,\rm Myr. \tag{34}$$

Phase 1 (≈ 60 Myr) — Active Fe-Ni Segregation. Constrained by the hafnium-tungsten (Hf-W) chronometer (Kleine et al., 2002; Yin et al., 2002): the core grows rapidly but the thermal gradient remains sub-adiabatic; no dynamo is possible during this phase.

Phase 2 (≈ 140 Myr) — Protocrust Formation. The growing Moon stabilizes obliquity at $\approx 23.5^\circ$; the protocrust forms around 4.4 Ga, as attested by the Jack Hills zircons (Wilde et al., 2001; Valley et al., 2002).

Phase 3 (≈ 150 Myr) — Progressive Dynamo Emergence. Compositional convection in the Fe-Ni core grows until the Lorentz force becomes comparable to the Coriolis force. The Elsasser number Λ balances these two forces. The threshold $B_{\rm crit} \approx 6\,\mu$T is derived in Appendix F. Modern geodynamo simulations (Christensen & Aubert, 2006; Olson & Christensen, 2006) show that the transition is gradual, not abrupt: $\Lambda \sim 1$ is an order-of-magnitude reference, not a strict threshold.

Established Result

A $\approx$ 350 Myr delay with no free parameter. Δt_{ej}: constrained by the Hf-W chronometer (Kleine et al., 2002; Yin et al., 2002). Δt_{cool}: constrained by the Jack Hills zircons at 4.4 Ga (Wilde et al., 2001; Valley et al., 2002). Δt_{em}: constrained by Tarduno et al. (2025) at 4.2 Ga. These are three independent observations, not an interpolation. The associated uncertainty is ± 50 Myr (L4).

8 Mass Balance: $N = 2$–3 Episodes

8.1 Corrected Target Lunar Mass

A fundamental point: the present-day observed lunar mass $M_{\text{Moon}} = 7.34 \times 10^{22}$ kg is *not* the mass that the TPT mechanism must produce. The Moon accreted additional mass after the ejection episodes:

- **South Pole–Aitken basin impactor:** a differentiated body roughly 260 km in diameter struck the Moon and *remained there*, contributing $M_{\text{SPA}} \approx 3.2 \times 10^{19}$ kg (Wakita et al., 2026). This material is now part of the observed lunar mass.
- **Late Hadean accretion:** documented late accretion contributed an additional mass ΔM_{late} (Zellner, 2019).

The target mass for the TPT mechanism is therefore:

$$M_{\text{TPT}} = M_{\text{Moon}} - M_{\text{SPA}} - \Delta M_{\text{late}} < 7.34 \times 10^{22}\,\text{kg}. \tag{35}$$

8.2 Mass Balance Equation

$$M_{\text{Moon}} = N \cdot f_{\text{cap}} \cdot M_{\text{éj}}^{\text{max}} + M_{\text{SPA}} + \Delta M_{\text{late}}, \tag{36}$$

with $N = 2$–3 (nominal), $f_{\text{cap}} \in [0.65, 0.85]$ (nominal 0.70), $M_{\text{éj}}^{\text{max}} \approx 2.0$–$4.0 \times 10^{22}$ kg per episode.

f_{cap}	$M_{\text{TPT}}^{(N=2)}$	$M_{\text{TPT}}^{(N=3)}$	Fraction of M_{Moon}
0.50	2.5×10^{22} kg	3.7×10^{22} kg	34–50%
0.70	3.5×10^{22} kg	5.2×10^{22} kg	48–71%
0.85	4.3×10^{22} kg	6.4×10^{22} kg	59–87%

The remainder is accounted for by M_{SPA} and documented late accretion. The balance is robust across the entire range of f_{cap}.

Established Result

f_{cap} is an increasing state variable. $\partial f_{\text{cap}}/\partial M_{\text{Moon}} > 0$: the larger the proto-Moon, the more efficiently it captures subsequent ejecta. This positive feedback, combined with the decrease of $g_{\text{eff}}^{(k)}$ at each episode, defines a dynamical attractor that reinforces the mechanism.

9 Chronology: Moon Formation in 3–4 Weeks

9.1 The Three Phases of an Episode

Each ejection episode comprises three phases:

1. **Resonant acceleration.** The CMT grows exponentially via elliptical instability (Section 5.5): $t_{\text{acc}} = \ln(U_{\text{crit}}/U_{\text{turb}})/\sigma_{\text{res}} \approx 1.4$ days.
2. **Ejection.** The flow crosses the Roche radius ($3R_{\text{eq,proto}} \approx 22.2$ Mm) at U_{crit}: $t_{\text{éj}} \approx 0.6$ hour.
3. **Recharging.** The CMT reorganizes over 5–6 nutation periods: $t_{\text{rec}} \approx$ 10–12 days.

The Fe-Ni segregation rate (Stokes' law) is nearly instantaneous between episodes ($\tau_{\text{Stokes}} \approx 254$ s), implying that each accreted layer is chemically distinct from the previous one — a direct consequence of the seismic prediction P1.

9.2 Complete Chronology

Phase	**Duration**	**Cumulative**
Episode 1: Acceleration	1.4 days	1.4 days
Episode 1: Ejection	0.6 h	1.4 days
Recharging (5–6 nutation periods)	10–12 days	11–13 days
Episode 2: Acceleration	1.4 days	12–14 days
Episode 2: Ejection	0.6 h	12–14 days
Recharging	10–12 days	22–26 days
Episode 3: Acceleration	1.4 days	23–27 days
Episode 3: Ejection	0.6 h	23–27 days
Total (N = 3)	**24–28 days**	

This 3–4-week timescale is the only intermediate temporal window between the giant impact (a few hours) and the synestia (~ 100 years) on the Hf-W chronometer (half-life: 8.9 Ma) — giving rise to Prediction P7.

Established Result

Chronology for N = 3 episodes.

1. Episode 1: acceleration ($\approx$ 1.4 days) + ejection ($\approx$ 0.6 h). Formation of the proto-POB, $R_1 \approx 1{,}560$ km.
2. Recharging + Episode 2: $\approx$ 11–13 days. Asymmetric episode: post-ejection transient precession alters ε, producing the crustal dichotomy.
3. Recharging + Episode 3: $\approx$ 11–13 days. The lunar mass is reconstituted.
4. Total duration: $\approx$ 24–28 days.
5. Closure of the TPT window: $t \approx 30$–50 Ma.
6. Onset of the Hadean dynamo: $t \approx 330$–350 Ma.

9.3 Age of the Moon: LMO Solidification versus Formation

The measured age (4.425 ± 0.025 Ga) is that of the solidification of the lunar magma ocean (LMO), not of formation. If the TPT is triggered at ≈ 4.467 Ga, LMO cooling (~ 40 Ma) gives a predicted solidification age:

$$t_{\mathrm{LMO}} \approx 4.467 - 0.040 = 4.427\,\mathrm{Ga}, \tag{37}$$

consistent at 0.1σ with the measured value. Prediction P8 is a formation age $>$ 4.45 Ga, directly testable by Artemis III.

Established Result

A rapid formation, in 3–4 weeks, datable by Hf-W. This timescale distinguishes the TPT from the giant impact and from the synestia; it further predicts a formation age ($\approx$ 4.467 Ga) earlier than the measured LMO solidification age (4.425 ± 0.025 Ga), the two being consistent once LMO cooling is taken into account.

10 Internal Stratification and Seismology Program

10.1 Architecture of Concentric Layers

Each ejected sheet originates from magma at a progressively more advanced stage of Fe-Ni segregation:

$$\left(\frac{\mathrm{Fe}}{\mathrm{Si}}\right)_{\text{layer } k} > \left(\frac{\mathrm{Fe}}{\mathrm{Si}}\right)_{\text{layer } k+1}, \tag{38}$$

since the source magma becomes progressively depleted in siderophile elements between episodes. Density contrasts between layers $\Delta\rho_{k,k+1} \approx 100$–$200\ \mathrm{kg\,m^{-3}}$ (Garcia et al., 2019) produce potentially detectable acoustic impedance contrasts.

10.2 Preservation Window: 200–530 km

Two destructive processes bound the preservation window:

From below: ilmenite cumulate overturn (Briaud et al., 2023) may have remelted the deepest layers (episodes 1–2, > 600 km).

From above: mare basalt volcanism, active until ≈ 2 Ga (Li et al., 2021; Che et al., 2021), remelted the shallowest layers (< 100 km).

The surviving preservation window is therefore approximately 200–530 km in depth.

10.3 Interface Depth: N=2 vs N=3

For N=2 with equal masses, the interface between the two layers lies at:

$$d = R_{\text{Moon}} - R_1 \approx 1{,}737 - 1{,}560 \approx 177\,\text{km} \quad (N = 2). \tag{39}$$

For N=3, the primary interface lies within the 200–315 km window. Chang'e 7 seismic data will therefore allow discrimination between $N = 2$ and $N = 3$.

Established Result

A testable, dated, and localized stratification. The Fe/Si gradient increasing with depth, the 200–530 km preservation window bounded by two independent destructive processes, and the position of the primary interface depending on $N = 2$ or $N = 3$ together constitute a directly discriminating seismology program.

11 Observational Constraints and Existing Evidence

11.1 Isotopic Identity Δ^{17}O < 5 ppm

The Earth–Moon isotopic composition is nearly identical for O, Cr, and Ti, established to better than 5 ppm (Wiechert et al., 2001; Dauphas et al., 2014; Dauphas, 2017; Sossi et al., 2025). The TPT satisfies this constraint *mechanically*: at each ejection episode, material is drawn from the contemporary Hadean terrestrial mantle, with no exogenous isotopic source. No *ad hoc* isotopic mixing is required.

11.2 Iron Depletion

The Moon is significantly less iron-rich than the terrestrial mantle (O'Neill, 1991; Jones & Drake, 1986). In the TPT, this depletion is a direct consequence of the single engine: at each successive episode, the ejected mantle is more depleted in siderophile elements than the previous one, since Fe-Ni segregation progressively removes iron from the source zone between episodes.

11.3 Angular Momentum

The angular momentum budget of the Earth–Moon system requires a rapidly rotating proto-Earth. The value $T_{\rm rot} = 3.5$ h is consistent with the median value from N-body accretion simulations (Agnor et al., 1999; Kokubo & Genda, 2010): rapid rotation is the norm at the end of accretion, not an exception.

11.4 Chang'e-6 Results: Preliminary Observational Support for P3 and P6

The Chang'e-6 mission returned 1,935 g of samples from the Apollo basin in the South Pole–Aitken (SPA) region in June 2024. Analysis of these samples provides preliminary support for two TPT predictions.

Norites at 4247 ± 5 Ma — Age of Episode 1. Yue et al. (2026) dated Chang'e-6 norite samples at 4247 ± 5 Ma using the Pb-Pb method. These norites are interpreted as differentiated products of the SPA impact melt sheet, representing deep lunar mantle material excavated by the SPA impact. This age is consistent with the TPT prediction that the innermost lunar layer (Episode 1) was accreted at ≈ 4.5 Ga and partially reset by the SPA impact at ≈ 4.25 Ga.

Anomalously High Fe/Mn in Deep Olivines — Signature of Episode 1's Fe-Rich Material. Xu et al. (2025) report olivine fragments in Chang'e-6 samples containing Fe and Mn concentrations significantly higher than those found in the standard lunar mantle. Zinc concentrations are $\approx 100\times$ higher than expected in the lunar mantle. While part of this enrichment is attributed to meteoritic contamination, the olivine fragments themselves formed through mixing of lunar rock and molten asteroid material. The elevated Fe content in material excavated at SPA depths is *consistent* with prediction P3 (Fe/Si gradient increasing with depth) and provides preliminary support for prediction P6.

Established Result

Four constraints satisfied with no tuning, plus initial observational support. Isotopic identity, iron depletion, and angular momentum are mechanical consequences of the single engine; the Chang'e-6 samples (norites at 4247 ± 5 Ma, high-Fe/Mn olivines) provide preliminary, not yet confirmatory, support for predictions P3 and P6.

12 Falsifiable Predictions

P1 — Seismic Interface at $d \approx 200$–315 km (Priority 1)

Concentric stratification produces acoustic impedance contrasts $|R| \in [0.01, 0.04]$ between layers. For N=2, the interface is at $d \approx 177$ km. For N=3, the primary interface is at $d \approx 200$–315 km.

Detectability with Chang'e-7 depends on the seismometer's sensitivity (target 10^{-8} m s^{-2} Hz$^{-1/2}$ at 0.1–1 Hz). This sensitivity should resolve $|R| > 0.01$, provided at least 10 events with $M > 2.5$ are recorded within the first 6 months of operation.

Falsification condition: no phase conversion detected within the 200–530 km window after deployment of at least 3 seismic stations and detection of at least 10 lunar events with $M > 2.5$.

Missions: Chang'e 7 (August 2026, South Pole seismometer), FSS (Farside Seismic Suite), LEMS (Lunar Environment Monitoring Station), Artemis III (2028–2029).

P2 — Near-Side / Far-Side Seismic Asymmetry

The second, asymmetric episode produces a sharper, deeper interface beneath the far side.

Falsification: spherical symmetry confirmed by a complete tomographic inversion.

P3 — Fe/Si Gradient Increasing with Depth

Fe/Si increases with depth in the lunar mantle, reflecting the progressive Fe-Ni depletion of the source magma between episodes. The SPA basin preferentially exposes Episode 1 material (the most Fe-rich).

Preliminary support: Chang'e-6 olivines with high Fe/Mn (Xu et al., 2025). *Missions:* Chang'e-6 (further analyses), Artemis III.

P4 — Dynamo Delay: 290–360 Ma

Progressive dynamo emergence predicts continuous paleointensity growth from 4.55 to 4.20 Ga, with no abrupt *onset* (Tarduno et al., 2025).

Falsification: an abrupt *onset* of the geomagnetic field detected in the Jack Hills zircon record.

P5 — Instability Window: $\varepsilon \in [57°, 70°]$

Parametric elliptical instability requires ε within this range.

Test: N-body simulations of telluric proto-planet obliquity.

P6 — Polar Ejecta Signature at High Latitudes

Wobble ejects material from all latitudes of the body frame. High-latitude ejecta preferentially concentrate at the South Pole during the second, asymmetric episode. Prediction: elevated Fe/Si ratio and a distinct seismic signal at the South Pole relative to equatorial Apollo sites.

Mission: Chang'e 7 (South Pole, August 2026).

P7 — Signature in the Hf-W Chronometer

A formation duration of 3–4 weeks is the only intermediate temporal window between the giant impact (a few hours) and the synestia ($\sim$ 100 years) on the Hf-W chronometer (half-life: 8.9 Ma). The ^{182}Hf/^{180}Hf ratio in Episode 1 samples should correspond to a differentiation age of 4.467 Ga (100 ± 10 Ma after CAIs), versus 60 ± 10 Ma for the giant impact (Kleine et al., 2002).

Mission: Artemis III (2028–2029).

P8 — Formation Age $>$ 4.45 Ga

The measured age of 4.425 Ga is that of LMO solidification, not of formation (Section 9). The formation age is ≈ 4.467 Ga.

Test: direct dating of Episode 1 rocks exposed on the central peaks of the SPA basin (Artemis III).

P9 — Mare Basalt Compatibility with Layer 1

The melting depth of mare basalts (200–500 km, ± 100 km) is compatible with a source in layer 1 ($> d_{\mathrm{P1}}$), without this being assertable in the absence of more precise geochemical data.

Test: high-resolution isotope geochemistry of Apollo and Chang'e-5 mare basalts (Li et al., 2021).

P10 — Seismic Interface at $d \approx 177$ km for $N = 2$ (Priority 2)

For $N = 2$ episodes of equal masses, the single interface between the two concentric layers lies at $d \approx 177$ km. This depth is outside the main preservation window (200–530 km) because it has been partially remelted by mare volcanism and/or ilmenite cumulate overturn. However, partial remnants could be detected as weak reflectors or seismic velocity variations in the 150–200 km zone.

13 Validation Windows: Three Imminent Tests

13.1 Chang'e 7: Imminent Seismic Validation (August 2026)

The Chang'e 7 mission (CNSA, planned launch August 2026) will deploy the first seismometer at the lunar South Pole since Apollo 17 (1972). Its data will provide a direct test of P1 and P6. The prediction is pre-registered and quantified: $d \approx 200$–315 km, $|R| \in [0.01, 0.04]$. The falsification criterion is explicit.

13.2 The South Pole–Aitken Basin: Stratigraphic Revealer

The SPA basin did not create the concentric lunar stratigraphy: it *excavated* it. The layered structure predated the SPA impact at ≈ 4.25 Ga (Yue et al., 2026), encoded during TPT differentiation at ≈ 4.5 Ga. The impact is the accidental revealer of a far older internal architecture.

High-resolution 3D simulations (Wakita et al., 2026) demonstrate that the north-to-south oblique trajectory of the SPA impactor projected deep mantle ejecta preferentially toward the South Pole in a butterfly-shaped plume — precisely the Artemis III landing zone. These same simulations predict ≈ 350 m of mantle material on average at this site, excavated from depths greater than 90 km, consistent with the TPT preservation window.

13.3 Artemis III: Direct Sampling of Episode 1 Material

The Artemis III mission (NASA, planned 2028–2029) will land astronauts near the Shackleton crater at the South Pole. According to Wakita et al. (2026), surface samples at this site may include deep mantle ejecta from the SPA impact. If so, these samples will allow a direct test of P3, P7, and P8: their Fe/Si ratio, crystallization age (≈ 4.467 Ga for primary Episode 1 material), and isotopic signature ($\Delta^{17}O < 5$ ppm relative to the contemporary terrestrial mantle) are all quantitative TPT predictions.

Established Result

Mission convergence. Chang'e 7 (2026): seismology, P1, P2, P6. Artemis III (2028): geochemistry, P3, P7, P8. Two independent space agencies, one unique geographic site, one internal architecture to confirm or refute.

14 Predicted Falsification Pathways

What Would Seriously Challenge the TPT

1. **No seismic interface within 200–530 km** after adequate station coverage (P1 falsified).

2. **Spherically symmetric lunar mantle** from complete tomographic inversion (P2 falsified).
3. **Abrupt dynamo onset** at ≈ 4.2 Ga rather than continuous growth (P4 falsified).
4. **SPA mantle ejecta Fe/Si no higher** than terrestrial peridotite or mare basalts after correction for impact mixing (P3 and P6 falsified).
5. **Hf-W age** incompatible with 100 ± 10 Ma after CAIs (P7 falsified).

Conversely, the TPT does **not** require:

- A specific initial rotation period other than the 2.5–4.0 h range.
- A unique value of f_{cap}; the mass balance is robust for $f_{\text{cap}} \in [0.5, 0.85]$.
- A fully intact ejected flow; partial fragmentation (L3) does not break the mechanism.
- A 3D SPH simulation prior to observational tests.

15 Discussion

15.1 Comparison with the Giant-Impact Model

Constraint	**Giant Impact**	**TPT (this work)**
Isotopic identity	Requires a very specific impactor composition and mixing conditions	Satisfied mechanically by construction
Fe depletion	Requires a pre-differentiated impactor (Theia)	Direct consequence of the single engine
Crustal dichotomy	Not naturally predicted	Qualitative prediction: post-Episode 2 precession (L7)
Dynamo delay	Not predicted	Proposed: $\approx$ 350 Myr, with no free parameter
Seismic predictions	None	P1 testable by Chang'e 7 (August 2026)
Chang'e-6 Fe anomaly	Not predicted	Consistent with P3 and P6 (Xu et al., 2025; Yue et al., 2026)
Formation timescale	A few hours	3–4 weeks
Hf-W signature	60 ± 10 Ma after CAIs	100 ± 10 Ma after CAIs (P7)

A recent review concludes that there is currently no unambiguous geochemical or isotopic evidence for the role of an external impactor in Moon formation (Sossi et al., 2025). This conclusion motivates the exploration of alternatives grounded in the internal dynamics of the proto-Earth.

15.2 Justification of $\alpha > 1$

Two independent mechanisms lead to a super-rigid rotation profile: differential equator-to-pole cooling generates a density gradient and thermal spin-up; Fe-Ni segregation lightens the CMT, and by angular momentum conservation, its inner part accelerates. The Bingham-Herschel threshold also suppresses small scales, favoring a block profile. Numerical validation of this profile is a 3D SPH simulation

priority.

15.3 Partial Fragmentation and Coalescence

Even if the ejected sheet partially fragments, the fragments remain within the same orbital zone and coalesce rapidly under inelastic collisions and gravitational attraction from the proto-POB (Canup & Asphaug, 2001). The effective capture efficiency remains high ($f_{\text{cap}} \geq 0.7$). A detailed analysis (Appendix H) shows that f_{cap} has a physical lower bound of approximately 0.45–0.55, independent of the BH cohesion hypothesis.

15.4 Responses to the Main Objections

Detailed responses to the main objections are given in Appendix I. Here are the key points:

"Equation (3) assumes instantaneous Earth formation." It is a thermodynamic bound, not a timescale. The total gravitational energy released exceeds the melting energy by a factor of 155, a result established by Solomatov (2000), Elkins-Tanton (2012), and Rubie et al. (2015).

"ε is the astronomical obliquity; there is no radial Coriolis force." ε is the angle in the body frame, defined in Section 1.5. The radial/horizontal decomposition of the Coriolis force follows directly from this geometry.

"The CMT has not been demonstrated." The CMT is the spatial expression of the $\ell = 1, m = 1$ mode of the geostrophic inverse cascade. Its quantitative validation requires a 3D SPH simulation (L1), but the theory does not depend on this for its observational tests.

"Taylor-Proudman prevents the CMT." The columns are curved by five mechanisms; their curvature generates the toroidal flow. The Taylor-Proudman constraint does not apply to the purely toroidal field (Frigaard & Nouar, 2017).

"The dynamo delay is arbitrary." It is the sum of three durations constrained by three independent observations (Section 7.3).

Established Result

An alternative that addresses the canonical model point by point. The structured comparison with the giant impact and the responses to the five main objections show that the TPT mechanically satisfies the geochemical constraints that the giant impact must tune, without resorting to a hypothetical external impactor.

16 Acknowledged Limitations

L1 — Spontaneous CMT Organization

Whether a single torus or several coexisting structures emerge in the exact Hadean regime can only be resolved by a high-resolution 3D SPH simulation with full BH rheology. **Priority 2.**

L2 — Numerical Value of f_{cap}

The capture efficiency $f_{\text{cap}} = 0.70$ is physically motivated but not derived from first principles. The 3D SPH simulation is the ultimate arbiter of this value and its dependence on M_{Moon} (Prediction P12: $\partial f_{\text{cap}}/\partial M_{\text{Moon}} > 0$).

L3 — Small-Scale Cohesion

The $\text{Bi}_{\text{KH}} \gg 1$ argument holds at large and intermediate scales. At very small scales ($\lambda_{\text{KH}} \ll R_{\text{torus}}$), partial fragmentation cannot be analytically excluded. However, fragments from the same toroidal flow, ejected at the same velocity and angle, find themselves on nearly identical orbits and accrete onto the POB: the mass balance is unaffected by fragmentation, only the fragment size.

L4 — Dynamo Delay: ± 50 Myr

The exponential core growth model is simplified; the associated uncertainty is ± 50 Myr.

L5 — Super-Rigid Profile $\alpha > 1$

The super-rigid rotation profile ($U \propto r^{\alpha}, \alpha > 1$) is physically motivated by differential rotation in a rapidly cooling partially crystallized magma, but has not been demonstrated under these exact Hadean conditions. This is a Level 3 hypothesis, to be validated by simulation.

L6 — Flow → POB Transition: Qualitative Status

The three-phase description of the ejected flow (ballistic expansion, orbital insertion, sticky accretion beyond R_{Roche}) is physically motivated and consistent with computed order-of-magnitude estimates, but remains qualitative. A 3D SPH simulation with coupled radiative cooling is required. **Priority 2b.**

L7 — Crustal Dichotomy: Qualitative Prediction

The $\approx 2:1$ thickness ratio is a qualitative prediction of the TPT. The coupled differential thermal calculation has not yet been derived analytically.

Additional context. The lunar far side underwent at least two independent remelting episodes that must be accounted for in any quantitative model: (1) the SPA basin-forming impact at ≈ 4.25 Ga, which excavated and partially remelted the deepest Episode 1 layer on the far side (Wakita et al., 2026); and (2) prolonged mare volcanism extending to ≈ 3.2 Ga (Li et al., 2021), which remelted the shallowest layers (< 100 km) over much of the far side. The net effect is to deepen and reinforce the existing asymmetry rather than erase it. Extruded rocks exposed on central peaks of SPA basin craters should preserve a geochemical record of pre-impact Episode 1 material: their composition (Fe/Si, Δ^{17}O) is expected to match the contemporary Hadean terrestrial mantle (prediction P3).

L8 — Rossby Wave Speed in a BH Fluid

The rigorous derivation of $c_{\text{Rossby}}^{(\text{BH})}$ for a BH fluid on an oblate spheroid ($\varepsilon \neq 0$) remains an open problem. The channel-analogy correction (factor ≈ 40) used here reinforces rather than invalidates the synchronization argument, but awaits a rigorous derivation.

L9 — Impact Mixing in SPA Ejecta

The geochemical signature of deep mantle material excavated by the SPA impact is potentially diluted or modified by mixing with impactor material and local crust. Quantitative deconvolution of the primary Episode 1 signature from impact-melt breccia requires detailed petrological and isotopic studies. This limitation affects predictions P3 and P6.

L10 — Deep Mantle Samples Predicted but Not Yet Retrieved

The TPT predicts that deep mantle material from Episode 1 is exposed on the central peaks of the South Pole–Aitken basin craters, excavated and extruded during the SPA impact at ≈ 4.25 Ga (Wakita et al., 2026). These samples are the primary targets for testing predictions P3 (Fe/Si gradient), P7 (Hf-W age), and P8 (formation age > 4.45 Ga). This prediction will be directly testable by **Chang'e 7** (South Pole seismology and remote sensing, August 2026) and **Artemis III** (direct sampling of SPA central peaks, 2028–2029). However, no sample from these central peaks has yet been retrieved or analyzed. The theory therefore makes a clear, falsifiable prediction that awaits these imminent missions. The absence of deep mantle material at the predicted locations, or a Fe/Si ratio inconsistent with P3, would seriously challenge the TPT.

17 Conclusion

This work proposes that Moon formation could be the product of a Triple Phase Transition within a fully molten proto-Earth rotating at ≈ 3.5 h, whose axis oscillates within $[40°, 70°]$ in its own co-rotating frame — a range supported by five convergent arguments, of which the first and most fundamental is the logically necessary absence of any tidal stabilizer. A single engine — progressive Fe-Ni segregation — simultaneously governs three transitions: rheological, mechanical, and magnetic. The result is a Moon built layer by layer in two to three massive episodes, each layer archiving in its internal structure the state of Hadean differentiation at the time of its accretion.

Parametric elliptical instability — established in fluid mechanics (Malkus, 1968; Kerswell, 2002; Lacaze et al., 2004) but never previously applied to lunar formation — amplifies the CMT to the bifurcation velocity in ≈ 32 hours. The generalized instability equation $\lambda_{\text{global}}(\varphi, \varepsilon, t)$ is valid at all latitudes of the body frame. A dedicated section addresses the maintenance of obliquity in the out-of-equilibrium Hadean context. A three-to-four-week chronology yields three new testable predictions (P6, P7, P8).

The mass balance is self-consistent without forcing: the target mass for the TPT mechanism is less than the present-day observed lunar mass, since the SPA impactor and late accretion contributed afterward. At $T_{\text{rot}} = 3.5$ h, the ejectable mass per episode can reach $\approx 70\%$ of the present lunar mass, which explains why $N = 2$–3 suffices.

Preliminary observational support comes from Chang'e-6: norites at 4247 ± 5 Ma (Yue et al., 2026) and olivines with high Fe/Mn (Xu et al., 2025) are consistent with predictions P3 and P6, though not yet confirmatory.

The central prediction remains: one or more seismic interfaces within the 200–530 km window (or at ≈ 177 km for N=2), testable by Chang'e 7 in August 2026. If an interface with $|R| > 0.02$ is detected within this window, concentric stratification receives its first strong observational support before any SPH simulation. If no interface is detected under the stated falsification conditions, prediction P1 is seriously challenged and the theory will require revision — which the author explicitly accepts.

This work invites the planetary science community to evaluate the TPT on its own terms: the equations are numbered, the derivations are explicit, the hypotheses are hierarchized, the limitations are acknowledged, and the predictions are falsifiable. The TPT will be judged primarily on its observational predictions — the Chang'e 7 seismic data (August 2026) and the Artemis III samples (2028–2029) — before and independently of any complete numerical validation.

A Adiabatic Temperature Profile

With $T_{\text{surf}} \approx 3{,}500$ K and an adiabatic gradient $\mathrm{d}T/\mathrm{d}r \approx -0.3\ \mathrm{K\,km^{-1}}$, the central temperature reaches $\approx 5{,}000$ K. The peridotite solidus at 135 GPa is $\approx 4{,}300$ K (Stixrude & Lithgow-Bertelloni, 2014): melting is thermodynamically stable throughout the mantle, confirming H0.

Established Result

The adiabatic profile confirms H0. The central temperature ($\approx 5{,}000$ K) exceeds the deep peridotite solidus ($\approx 4{,}300$ K at 135 GPa), validating total volumetric melting of the silicate mantle.

B Demonstration of the $b' = 1$ Attractor

The parameter b' is defined as the ratio between the critical ejection velocity U_{crit} and the geostrophic equilibrium velocity U_{eq}:

$$b' = \frac{U_{\text{crit}}}{U_{\text{eq}}} = \frac{2\Omega \sin\varepsilon \sqrt{2|g_{\text{eff}}| R_{\text{éq,proto}}}}{|g_{\text{eff}}|}. \tag{40}$$

Evolution Due to Fe-Ni Segregation. The CMT's density decreases as $\rho_{\text{TMC}}(t) = \rho_0(1 - \xi_{\text{Fe}}(t))$, where $\xi_{\text{Fe}}(t)$ is the segregated Fe-Ni fraction. Effective gravity $|g_{\text{eff}}|$ is proportional to ρ_{TMC}: $|g_{\text{eff}}| \propto \rho_{\text{TMC}}$. Thus,

$$\left.\frac{\mathrm{d}b'}{\mathrm{d}t}\right|_{\text{segregation}} = \frac{1}{2}\frac{\dot{\rho_{\text{TMC}}}}{\rho_{\text{TMC}}}\, b' > 0, \tag{41}$$

since $\dot{\rho_{\text{TMC}}} < 0$.

Evolution Due to Ejection. An ejection carries away a fraction $\epsilon = M_{\text{éj}}^{\max}/M_{\text{TMC}} \approx 0.1$ of the CMT's mass. Angular momentum decreases as $\Delta\Omega/\Omega \approx -\epsilon$. Effective gravity decreases as $\Delta|g_{\text{eff}}|/|g_{\text{eff}}| \approx -\epsilon$ (proportional to the lost mass). Thus,

$$\left.\frac{\Delta b'}{b'}\right|_{\text{ejection}} = \frac{\Delta\Omega}{\Omega} - \frac{1}{2}\frac{\Delta|g_{\text{eff}}|}{|g_{\text{eff}}|} \approx -\epsilon + \frac{1}{2}\epsilon = -\frac{1}{2}\epsilon < 0. \tag{42}$$

Stable Fixed Point. The two tendencies oppose each other: segregation increases b', ejection decreases it. The equilibrium point $b' = 1$ is a stable attractor. For $b' < 1$, the system is unstable and an ejection occurs, which decreases b' (since $\Delta b' < 0$). For $b' > 1$, the system is stable, no ejection occurs, and segregation increases b' toward 1 from below. The point $b' = 1$ is therefore a stable attractor.

Established Result

$b' = 1$ **is a dynamical attractor of the coupled system.** Fe-Ni segregation and ejection drive b' in opposite directions; their opposition stabilizes the system around $b' = 1$, naturally selecting $T_{\text{rot}} \approx 3.5$ h and $\varepsilon \approx 55°$.

C Complete Derivation of the λ Coefficient

Application of the Solberg-Høiland parcel-displacement formalism (Solberg, 1936; Høiland, 1941) to an oblate sphere with obliquity ε. Angular momentum conservation ($\tau_{\text{relax}}/\tau_{\text{dyn}} \approx 3 \times 10^9 \gg 1$):

The parcel conserves its specific angular momentum $L = U \cdot r$:

$$U_{\text{parcel}}(r + \xi_r) = \frac{U(r) \cdot r}{r + \xi_r} \approx U(r)\left(1 - \frac{\xi_r}{r}\right), \tag{43}$$

The background flow at the new position, with profile $U(r) \propto r^\alpha$:

$$U_{\text{bg}}(r + \xi_r) = U(r)\left(1 + \frac{\xi_r}{r}\right)^\alpha \approx U(r)\left(1 + \alpha\frac{\xi_r}{r}\right), \tag{44}$$

The velocity difference is therefore:

$$\delta U = U_{\text{parcel}} - U_{\text{bg}} = U(r)\left(1 - \frac{\xi_r}{r}\right) - U(r)\left(1 + \alpha\frac{\xi_r}{r}\right) = -U(r)(1+\alpha)\frac{\xi_r}{r}. \tag{45}$$

The net radial force sums three terms: effective gravity ($-g_{\text{eff}}^{(k)}\xi_r$), radial Coriolis ($+2\Omega^{(k)}\sin\varepsilon \cdot U\xi_r$), and the angular-momentum gradient term ($-U^2(1+\alpha)\xi_r/r^2$). The latter is always stabilizing for any physical profile ($\alpha > -1$), consistent with the classical Rayleigh stability criterion. Equation (30) follows with $a = -(1+\alpha)/r^2$.

Established Result

The coefficient λ derives directly from Solberg–Høiland. Conservation of the fluid parcel's angular momentum, combined with a background profile $U \propto r^{\alpha}$, supplies every term of Eq. (30) with no additional free parameter.

D Double Potential Well and Kramers Rate

Integrating $\lambda(U) = -\mathrm{d}V/\mathrm{d}U$, one obtains the CMT's effective potential:

$$V(U) = -\tfrac{a}{3}U^3 - \tfrac{b}{2}U^2 - cU + V_0. \tag{46}$$

For typical Hadean parameters ($a > 0, b > 0, c < 0$), $V(U)$ exhibits two extrema: a local minimum (confined well P_1) and a local maximum (barrier), followed by a second local minimum (ejective well P_2). The barrier height is $\Delta E_{\text{barr}} = V(U_{\text{peak}}) - V(U_{P_1})$.

The Kramers crossing rate (Kramers, 1940) is:

$$\Gamma_{\text{Kramers}} = \frac{\omega_0 \omega_b}{2\pi\gamma_{\text{diss}}} \exp\left(-\frac{\Delta E_{\text{barr}}}{k_B T_{\text{eff}}}\right), \tag{47}$$

where $\omega_0 = \sqrt{|V''(U_{P_1})|}$ and $\omega_b = \sqrt{|V''(U_{\text{peak}})|}$. The number of stochastic opportunities $N_{\text{opp}} \sim 10^9$–10^{10} ensures that the probability of no crossing is negligible.

Established Result

The double well transforms ejection into thermally activated crossing. Integrating $\lambda(U)$ naturally produces two extrema; the Kramers rate, combined with $\sim 10^9$–10^{10} stochastic opportunities, renders barrier crossing nearly certain throughout the TPT's active window.

E Demonstration of the $\mathrm{Bi}_{\mathrm{KH}}$ Criterion

The Bingham-Kelvin-Helmholtz number compares the yield stress to the KH shear stress:

$$\mathrm{Bi}_{\mathrm{KH}} = \frac{\tau_y\, k}{\rho\, \sigma_{\mathrm{KH}}\, \Delta U}, \tag{48}$$

where k is a geometric factor (~ 1), $\sigma_{\mathrm{KH}} \sim \Delta U/\lambda$ is the KH growth rate, and λ is the perturbation wavelength. Thus,

$$\mathrm{Bi}_{\mathrm{KH}} \sim \frac{\tau_y\, \lambda}{\rho\, \Delta U^2}. \tag{49}$$

For the CMT: $\tau_y \sim 10^2$–10^4 Pa, $\lambda \sim R_{\text{torus}} \sim 10^7$ m, $\rho \sim 3{,}000\,\text{kg}\,\text{m}^{-3}$, $\Delta U \sim U_{\text{crit}} \sim 10^4\,\text{m}\,\text{s}^{-1}$. One obtains $\text{Bi}_{\text{KH}} \sim 10^{-1}$–$10^1$, i.e. $\mathcal{O}(1)$ or greater. Cohesion is maintained through three reinforcements: (1) atmospheric pressure $P \sim 10^5$–10^7 Pa, (2) internal crystalline network multiplying fragmentation resistance by a factor of 3–10, (3) Rayleigh-Taylor suppression ($\rho_{\text{flow}}/\rho_{\text{atm}} \sim 200$).

Established Result

$\text{Bi}_{\text{KH}} \sim \mathcal{O}(1)$ **or greater, reinforced by three independent mechanisms.** The Bingham-Herschel threshold, combined with atmospheric confinement, the internal crystalline network, and Rayleigh-Taylor suppression, suffices to maintain toroidal flow cohesion despite a Weber number that would exclude cohesion for a free-streaming flow.

F Derivation of the Elsasser Number and B_{crit}

Balancing Coriolis force $F_C \sim 2\rho\Omega U$ and Lorentz force $F_L \sim B^2/(\mu L)$, with $\eta \sim UL$ (magnetic Reynolds number of order unity at the dynamo threshold):

$$B^2 \sim 2\mu\rho\Omega\eta, \qquad \Rightarrow \qquad \Lambda \equiv \frac{B^2}{\rho\mu\eta\Omega} \sim 2, \tag{50}$$

i.e. $\Lambda \sim \mathcal{O}(1)$. Using $\eta = (\mu_0\sigma)^{-1}$ with $\sigma \approx 5 \times 10^5\,\text{S}\,\text{m}^{-1}$, $\mu_0 = 4\pi \times 10^{-7}\,\text{H}\,\text{m}^{-1}$, $\rho \approx 10^4\,\text{kg}\,\text{m}^{-3}$, $\Omega \approx 4.99 \times 10^{-4}\,\text{rad}\,\text{s}^{-1}$, one obtains $B_{\text{crit}} \approx 6\,\mu\text{T}$.

Established Result

$B_{\text{crit}} \approx 6\,\mu$**T derives from the Coriolis–Lorentz balance.** The Elsasser number $\Lambda \sim \mathcal{O}(1)$ sets the threshold at which the Lorentz force becomes comparable to the Coriolis force in the core, with no parameter tuned beyond the physical properties of the Fe-Ni core.

G Fe-Ni Stokes Sedimentation Timescale

Stokes settling velocity for a Fe-Ni droplet of radius $r \approx 5$ cm in molten silicate:

$$v_{\text{Stokes}} = \frac{2}{9}\frac{(\rho_{\text{Fe}} - \rho_{\text{sil}})\, g_{\text{eff}}^{(0)}\, r^2}{\eta} \approx \frac{2}{9}\frac{3{,}300 \times 6.42 \times (0.05)^2}{0.1} \approx 118\,\text{m}\,\text{s}^{-1}. \tag{51}$$

Over a characteristic sedimentation distance $\ell \approx 30$ km: $\tau_{\text{Stokes}} = \ell/v_{\text{Stokes}} \approx 254$ s. Robust for $r \in [1, 10]$ cm and $\eta \in [0.05, 1]$ Pa s.

Established Result

Fe-Ni segregation is nearly instantaneous between episodes. $\tau_{\text{Stokes}} \approx 254\,\text{s}$, robust over the entire realistic range of droplet radius and viscosity: each accreted layer is therefore chemically distinct from the previous one.

H Accretion of Magmatic Ejecta: Why Perfect Cohesion Is Not Required

A recurring objection to the TPT mechanism concerns the cohesion of the ejected CMT flow during transit between the proto-Earth's surface and the Roche radius. This appendix demonstrates that, even without perfect flow cohesion, the physical properties of the ejected magma and orbital mechanics guarantee accretion into a single body.

H.1 Magma Is Not Dust

The ejected material is silicate magma at $T \approx 3{,}000$–$4{,}000$ K. Its dynamic viscosity is $\eta \approx 1$–100 Pa s (Giordano et al., 2008) — comparable to warm honey. Unlike solid rock fragments or a gas cloud, high-temperature magma does not disperse: it deforms and stretches, but remains dense and cohesive at the macroscopic scale. Two sticky magma blocks at low relative velocity do not rebound — they merge. Viscous coalescence replaces mechanical cohesion as the dominant aggregation mechanism once the flow has fragmented.

H.2 Orbital Concentration

Ejecta from the same TPT episode share, to first order, the same initial orbital energy budget. By conservation of energy and angular momentum, they populate a band of neighboring orbits rather than dispersing isotropically over 4π steradians. This orbital concentration is fundamentally different from an isotropic explosion: it is the same physical principle that produces accretion disks from tidally disrupted bodies.

The toroidal geometry of the CMT reinforces this effect: ejection occurs preferentially within the oblique intertropical band $|\phi| < 30°$, concentrating ejecta within a limited azimuthal solid angle. The resulting debris field is geometrically thin, maximizing mutual encounter rates.

H.3 Beyond the Roche Radius: Accretion Is Inevitable

Beyond the Roche radius $R_{\text{Roche}} = 2.456 R_{\oplus}$, the self-gravity of the ejecta cloud overcomes tidal disruption. For co-orbital magma fragments with total mass $M_{\text{cloud}} \approx$

2–4×10^{22} kg, the gravitational accretion timescale is:

$$\tau_{\text{acc}} \approx \frac{1}{\sqrt{G\rho_{\text{cloud}}}} \approx 10^3\text{–}10^5 \text{ yr}, \tag{52}$$

far shorter than the magma's thermal lifetime ($\tau_{\text{cool}} \sim 10^6$–$10^7$ yr for a lunar-size body, Elkins-Tanton 2008).

Throughout this accretion window, the magma remains above its solidus: each collision is plastic, not elastic. There is no fragmentation cascade, no rebound loss. The capture efficiency f_{cap} therefore has a physical lower bound independent of the BH cohesion hypothesis:

$$f_{\text{cap}}^{\text{min}} \approx \frac{M_{\text{cloud}}(r > R_{\text{Roche}})}{M_{\text{ej}}^{\text{total}}} \gtrsim 0.45\text{–}0.55, \tag{53}$$

the lost fraction (≈ 45–55%) corresponding to ejecta that fall back onto the proto-Earth or escape on hyperbolic orbits.

H.4 Implication for the Theory

The capture efficiency $f_{\text{cap}} = 0.70$ adopted in the main text is therefore not a free parameter the theory must defend at all costs. Even in the pessimistic scenario where the CMT flow completely fragments upon ejection, orbital mechanics and magma viscosity guarantee accretion of the co-orbital debris cloud beyond the Roche radius.

The critical question shifts from "does the flow remain cohesive?" to "what fraction of ejecta reaches the Roche radius?" — a question that depends on the ejection velocity distribution, not on BH rheology. This reformulation makes the theory more robust: cohesion is advantageous, but not necessary.

Established Result

Perfect flow cohesion is not required. Magma viscosity, orbital concentration, and self-gravity beyond the Roche radius together guarantee a capture efficiency $f_{\text{cap}}^{\text{min}} \gtrsim 0.45$–$0.55$, independently of any assumption about toroidal flow cohesion.

I Detailed Responses to Objections

Objection 1 — Equation (3) assumes instantaneous formation. Equation (3) is an *energetic thermodynamic bound*, not a formation timescale. It asks: does the total gravitational energy released during accretion, however slow, exceed the energy needed to melt the mantle? The answer, established by Solomatov (2000), Elkins-Tanton (2012), and Rubie et al. (2015), is yes by a factor of 155. The ≈ 30 Myr core-

formation timescale (Kleine et al., 2002) is explicitly incorporated into the TPT chronology as Δt_{ej} (Section 7.3).

Objection 2 — ε is the astronomical obliquity. ε is the angle in the body frame between $\boldsymbol{\Omega}$ and the principal axis of inertia of the Maclaurin spheroid — an internal geometric quantity with no reference to the ecliptic plane. The decomposition of the Coriolis force into radial and horizontal components (Eqs. 16–17) follows directly from this geometry.

Objection 3 — The CMT has not been demonstrated. The CMT is the spatial expression of the $\ell = 1$, $m = 1$ mode of the geostrophic inverse cascade at the Rhines scale in a rapidly rotating oblate body with $\varepsilon > 45°$. Four independent physical effects converge on the band $|\phi| < 30°$ as an attractor (Section 3). Quantitative validation requires a 3D SPH simulation (Priority 2), but the theory does not depend on this for its observational tests.

Objection 4 — Taylor-Proudman prevents the CMT. The columns exist but are curved by five mechanisms (Section 5). Their curvature generates the toroidal flow rather than inhibiting it. The Taylor-Proudman constraint does not apply to the purely toroidal field (Frigaard & Nouar, 2017).

Objection 5 — The dynamo delay is arbitrary. It is the sum of three durations constrained by three independent observations: (1) Hf-W chronometer (Kleine et al., 2002; Yin et al., 2002), (2) Jack Hills zircons (Wilde et al., 2001; Valley et al., 2002), (3) Tarduno et al. (2025).

Established Result

Five objections, five responses grounded in results already established in the main text. No response introduces a new hypothesis: each refers back to a derivation, a geometric definition, or an observational constraint already presented in the main text.

J List of Abbreviations

BH Bingham-Herschel, rheological law.

BiKH Bingham-Kelvin-Helmholtz number.

CME Coronal Mass Ejection.

CMT Coherent Magmatic Torus.

FSS Farside Seismic Suite.

Hf-W Hafnium-tungsten chronometer.

LHB Late Heavy Bombardment (≈ 3.9 Ga).

LEMS Lunar Environment Monitoring Station.

LMO Lunar Magma Ocean.

POB Proto-Orbiting Body.

SPA South Pole–Aitken (basin).

SPH Smoothed Particle Hydrodynamics.

TPT Triple Phase Transition.

References

Agnor, C. B., Canup, R. M., & Levison, H. F. (1999). On the character and consequences of large impacts in the late stage of terrestrial planet formation. *Icarus*, 142, 219–237.

Airapetian, V. S., Glocer, A., Gronoff, G., Hébrard, E., & Danchi, W. (2016). Prebiotic chemistry and atmospheric warming of early Earth by an active young Sun. *Nature Geoscience*, 9, 452–455.

Balmforth, N. J., & Craster, R. V. (2001). Non-Newtonian effects in the dynamics of a thin film. *Journal of Fluid Mechanics*, 426, 297–323.

Bingham, E. C. (1922). *Fluidity and Plasticity*. McGraw-Hill, New York.

Bouvier, J., Matt, S. P., Mohanty, S., et al. (2014). Angular momentum evolution of young low-mass stars and brown dwarfs. In *Protostars and Planets VI*, pp. 433–450. University of Arizona Press, Tucson.

Briaud, A., Ganino, C., Fienga, A., et al. (2023). The lunar solid inner core and the mantle overturn. *Nature*, 617, 743–746.

Canup, R. M., & Asphaug, E. (2001). Origin of the Moon in a giant impact near the end of the Earth's formation. *Nature*, 412, 708–712.

Canup, R. M. (2012). Forming a Moon with an Earth-like composition via a giant impact. *Science*, 338, 1052–1055.

Caricchi, L., Burlini, L., Ulmer, P., et al. (2007). Non-Newtonian rheology of crystal-bearing magmas and implications for magma ascent dynamics. *Earth and Planetary Science Letters*, 264, 402–419.

Chambers, J. E. (2001). Making more terrestrial planets. *Icarus*, 152, 205–224.

Chambers, J. E. (2013). Late-stage planetary accretion including hit-and-run collisions and fragmentation. *Icarus*, 224, 43–56.

Chandrasekhar, S. (1969). *Ellipsoidal Figures of Equilibrium*. Yale University Press, New Haven.

Che, X., Nemchin, A., Liu, D., et al. (2021). Age and composition of young basalts on the Moon, sampled by the Chang'e-5 mission. *Science*, 374, 887–890.

Christensen, U. R., & Aubert, J. (2006). Scaling properties of convection-driven dynamos in rotating spherical shells and application to planetary magnetic fields. *Geophysical Journal International*, 166, 97–114.

Ćuk, M., & Stewart, S. T. (2012). Making the Moon from a fast-spinning Earth : a giant impact followed by resonant despinning. *Science*, 338, 1047–1052.

Dauphas, N., et al. (2014). Geochemical arguments for an Earth-like Moon-forming impactor. *Philosophical Transactions of the Royal Society A*, 372, 20130244.

Dauphas, N. (2017). The isotopic nature of the Earth's accreting material through time. *Nature*, 541, 521–524.

Elkins-Tanton, L. T. (2008). Linked magma ocean solidification and atmospheric growth for Earth and Mars. *Earth and Planetary Science Letters*, 271, 181–191.

Elkins-Tanton, L. T., et al. (2011). Chondritic late accretion to Earth and Mars. *Earth and Planetary Science Letters*, 304, 326–336.

Elkins-Tanton, L. T. (2012). Magma oceans in the inner solar system. *Annual Review of Earth and Planetary Sciences*, 40, 113–139.

Feigelson, E. D., & Montmerle, T. (1999). High-energy processes in young stellar objects. *Annual Review of Astronomy and Astrophysics*, 37, 363–408.

Flasar, F. M., & Birch, F. (1973). Energetics of core formation : a correction. *Journal of Geophysical Research*, 78, 6101–6114.

Frigaard, I. A., & Nouar, C. (2017). Viscoplastic fluids : from theory to application. In *Viscoplastic Fluids : From Theory to Application*, pp. 201–238. Springer.

Garcia, R. F., Khan, A., Drilleau, M., et al. (2019). Lunar seismology : an update on interior structure models. *Space Science Reviews*, 215, 50.

Giordano, D., Russell, J. K., & Dingwell, D. B. (2008). Viscosity of magmatic liquids : a model. *Earth and Planetary Science Letters*, 271, 123–134.

Hamano, K., Abe, Y., & Genda, H. (2013). Emergence of two types of terrestrial planet on solidification of magma ocean. *Nature*, 497, 607–610.

Hekinian, R., et al. (1989). Intraplate abyssal volcanism. *Earth-Science Reviews*, 25, 213–251.

Herschel, W. H., & Bulkley, R. (1926). Konsistenzmessungen von Gummi-Benzollösungen. *Kolloid-Zeitschrift*, 39, 291–300.

Høiland, E. (1941). On the interpretation and application of the circulation theo-

rems of V. Bjerknes. *Avhandlinger Norske Videnskaps-Akademi Oslo*, 11, 1–24.

Huss, G. R., et al. (2009). Presolar grains in primitive meteorites and the compositions of their stellar sources. *Geochimica et Cosmochimica Acta*, 73, 4922–4945.

Jones, J. H., & Drake, M. J. (1986). Geochemical constraints on core formation in the Earth. *Nature*, 322, 221–228.

Kerswell, R. R. (2002). Elliptical instability. *Annual Review of Fluid Mechanics*, 34, 83–113.

Kleine, T., Münker, C., Mezger, K., & Palme, H. (2002). Rapid accretion and early core formation on asteroids and the terrestrial planets from Hf-W chronometry. *Nature*, 418, 952–955.

Kokubo, E., & Genda, H. (2010). Formation of terrestrial planets from protoplanets under a realistic accretion condition. *Astrophysical Journal Letters*, 714, L21–L25.

Königl, A. (1991). Disk accretion onto magnetic T Tauri stars. *Astrophysical Journal Letters*, 370, L39–L43.

Kramers, H. A. (1940). Brownian motion in a field of force and the diffusion model of chemical reactions. *Physica*, 7, 284–304.

Lacaze, L., Le Gal, P., & Le Dizès, S. (2004). Elliptical instability in a rotating spheroid. *Journal of Fluid Mechanics*, 505, 1–22.

Laskar, J., Joutel, F., & Robutel, P. (1993). Stabilization of the Earth's obliquity by the Moon. *Nature*, 361, 615–617.

Laskar, J., & Robutel, P. (1993). The chaotic obliquity of the planets. *Nature*, 361, 608–612.

Lebrun, T., Massol, H., Chassefière, E., et al. (2013). Thermal evolution of an early magma ocean in interaction with the atmosphere. *Journal of Geophysical Research: Planets*, 118, 1155–1176.

Li, G., & Batygin, K. (2014). On the spin-axis dynamics of a moonless Earth. *Astrophysical Journal*, 795, 67.

Li, Q. L., Zhou, Q., Liu, Y., et al. (2021). Two-billion-year-old volcanism on the Moon from Chang'e-5 basalts. *Nature*, 600, 54–58.

Mader, H. M., Llewellin, E. W., & Mueller, S. P. (2013). The rheology of two-phase magmas : a review and analysis. *Journal of Volcanology and Geothermal Research*, 257, 135–166.

Malkus, W. V. R. (1968). Precession of the Earth as the cause of geomagnetism. *Science*, 160, 259–264.

McLachlan, N. W. (1947). *Theory and Application of Mathieu Functions*. Clarendon

Press, Oxford.

Nomura, R., Ozawa, H., Tateno, S., et al. (2011). Spin crossover and iron-rich silicate melt in the Earth's deep mantle. *Nature*, 473, 199–202.

O'Neill, H. S. C. (1991). The origin of the Moon and the early history of the Earth — a chemical model. *Geochimica et Cosmochimica Acta*, 55, 1135–1157.

Olson, P., & Christensen, U. R. (2006). Dipole moment scaling for convection-driven planetary dynamos. *Earth and Planetary Science Letters*, 250, 561–571.

Poincaré, H. (1910). Sur la précession des corps déformables. *Bulletin Astronomique*, 27, 321–356.

Rhines, P. B. (1975). Waves and turbulence on a beta-plane. *Journal of Fluid Mechanics*, 69, 417–443.

Rubie, D. C., Melosh, H. J., Reid, J. E., et al. (2003). Mechanisms of metal-silicate equilibration in the terrestrial magma ocean. *Earth and Planetary Science Letters*, 205, 239–255.

Rubie, D. C., Jacobson, S. A., et al. (2015). Accretion and differentiation of the terrestrial planets with implications for the compositions of early-formed Solar System bodies and accretion of water. *Icarus*, 248, 89–108.

Safronov, V. S. (1969). *Evolution of the Protoplanetary Cloud*. Nauka, Moscow.

Schneider, J. M., & Kleine, T. (2025). The age and early evolution of the Moon revealed by the Rb-Sr systematics of lunar ferroan anorthosites. *Earth and Planetary Science Letters*, 669, 119592.

Shu, F. H., Najita, J., Ostriker, E., et al. (1994). Magnetocentrifugally driven flows from young stars and disks. *Astrophysical Journal*, 429, 781–796.

Solberg, H. (1936). Le mouvement d'inertie de l'atmosphère stable et son rôle dans la théorie des cyclones. *Météorologie*, 12, 121.

Solomatov, V. S. (2000). Fluid dynamics of a terrestrial magma ocean. In *Origin of the Earth and Moon*, pp. 323–338. University of Arizona Press, Tucson.

Sossi, P. A., et al. (2025). The Moon-forming giant impact. *Treatise on Geochemistry*, 3^{e} éd., 3, 417–479.

Stixrude, L., & Lithgow-Bertelloni, C. (2014). Thermal expansivity, heat capacity and bulk modulus of the mantle. *Philosophical Transactions of the Royal Society A*, 372, 20130076.

Sukoriansky, S., Dikovskaya, N., & Galperin, B. (2007). On the arrest of inverse energy cascade and the Rhines scale. *Journal of the Atmospheric Sciences*, 64, 3312–3327.

Tarduno, J. A., Zhou, T., Huang, W., & Jodder, J. (2025). Ancient geodynamo

recorded in Jack Hills zircons. *National Science Review*, 12, nwaf082.

Touma, J., & Wisdom, J. (1993). The chaotic obliquity of the planets. *Science*, 259, 1294–1297.

Tsiganis, K., Gomes, R., Morbidelli, A., & Levison, H. F. (2005). Origin of the orbital architecture of the giant planets of the Solar System. *Nature*, 435, 459–461.

Urey, H. C. (1955). The cosmic abundances of potassium, uranium, and thorium and the heat balances of the Earth, the Moon, and Mars. *Proceedings of the National Academy of Sciences*, 41, 127–144.

Valley, J. W., Peck, W. H., King, E. M., & Wilde, S. A. (2002). A cool early Earth. *Geology*, 30, 351–354.

Wakita, S., Johnson, B. C., Andrews-Hanna, J. C., Gowman, G., Davison, T. M., Collins, G. S., Bill, C. A., Marchi, S., Alexander, A. M., & Evans, A. J. (2026). A southward differentiated impactor forms the tapered shape of the South Pole–Aitken impact basin on the Moon. *Science Advances*, 12(19), DOI: 10.1126/sciadv.aea1984.

Wiechert, U., Halliday, A. N., Lee, D.-C., et al. (2001). Oxygen isotopes and the Moon-forming giant impact. *Science*, 294, 345–348.

Wieczorek, M. A., Neumann, G. A., Nimmo, F., et al. (2013). The crust of the Moon as seen by GRAIL. *Science*, 339, 671–675.

Wilde, S. A., Valley, J. W., Peck, W. H., & Graham, C. M. (2001). Evidence from detrital zircons for the existence of continental crust and oceans on the Earth 4.4 Gyr ago. *Nature*, 409, 175–178.

Xu, Y.-G., et al. (2025). Extralunar material in Chang'e-6 samples from the South Pole-Aitken basin farside. *Proceedings of the National Academy of Sciences*, 122, e2418136121.

Yin, Q., Jacobsen, S. B., Yamashita, K., et al. (2002). A short timescale for terrestrial planet formation from Hf-W chronometry of meteorites. *Nature*, 418, 949–952.

Yue, Z., Gou, S., Wang, Y., et al. (2026). Lunar chronology model with the Chang'e-6 farside samples and implications for the early impact history. *Science Advances*, 12(6), eady9265. DOI: 10.1126/sciadv.ady9265.

Zellner, N. E. B. (2019). Cataclysm no more : new views on the timing and delivery of lunar impactors. *Origins of Life and Evolution of Biospheres*, 49, 261–274.

Zuber, M. T., et al. (2013). Gravity field of the Moon from the Gravity Recovery and Interior Laboratory (GRAIL) mission. *Science*, 339, 668–671.